Synergy between turbulent and collisional transport in global Lagrangian gyrokinetic PIC simulations

T. Vernay[1], S. Brunner[1], L. Villard[1], B. F. McMillan[2], S. Jolliet[1], T. M. Tran[1], A. Bottino[3]

[1] *Centre de Recherches en Physique des Plasmas,*

Ecole Polytechnique Fédérale de Lausanne,

Association EURATOM – Confédération Suisse, CH-1015 Lausanne, Switzerland

[2] *Centre for Fusion, Space and Astrophysics,*

Department of Physics, University of Warwick,

Coventry CV4 7AL, United Kingdom

[3] *Max-Planck-Institut für Plasmaphysik, Boltzmannstrasse 2,*

EURATOM Association, D-85748 Garching, Germany

Abstract

Based on the CYCLONE case [A. M. Dimits *et al.*, Phys. Plasmas **7**, 969 (2000)], simulations of collisional electrostatic ITG microturbulence carried out with the global gyrokinetic Particle-In-Cell (PIC) code ORB5 [S. Jolliet *et al.*, Comp. Phys. Comm. **177**, 409 (2007)] are presented. Considering adiabatic electrons, an increase in ion heat transport over the collisionless turbulent case due to ion-ion collisions is found to exceed the neoclassical contribution. This synergetic effect is due to interaction of collisions, turbulence and zonal flows. The Dimits shift softening by collisions [Z. Lin *et al.*, Phys. Rev. Lett. **83**, 3648 (1999)] is further characterized. Turbulence simulations start from a neoclassical equilibrium [T. Vernay *et al.*, Phys. Plasmas **17**, 122301 (2010)] and are carried out over significant turbulence times thanks to a coarse-graining procedure [Y. Chen and S. E. Parker, Phys. Plasmas **14**, 082301 (2007)], ensuring a sufficient signal/noise ratio even at late times in the simulation. The relevance of the Lorentz approximation for ion-ion collisions, compared to a linearized Landau self-collision operator, is finally addressed in the frame of both neoclassical and turbulence studies.

I. INTRODUCTION

The effect of the radial electric field related to axisymmetric modes and the associated zonal flows on tokamak microturbulence has been widely studied in the frame of gyrokinetic simulations. In particular, the ITG turbulence saturation due to vortice shearing produced by zonal flows is a well established mechanism which reduces the turbulent transport in ITG-dominated regimes [1] [2] [3] [4]. Due to the high temperatures in the core of tokamak plasmas, collisionless gyrokinetic models have extensively been used for turbulent transport analysis. However, eventhough collisionality is not *a priori* a dominant effect for the core tokamak physics, it may nonetheless significantly affect the transport in at least three ways. First, collisions produce an intrinsical neoclassical transport. Usually small compared to the turbulent transport, neoclassical transport may nevertheless reach comparable levels, in conditions of marginal stability of microinstabilities. Secondly, collisions *damp* radial perturbations and associated zonal flows as predicted in Ref. [5]. Thirdly, collisions may in fact also *generate* a neoclassical radial electric field for ensuring ambipolarity in the presence of density and temperature gradients, leading to background $\vec{E} \times \vec{B}$ flows. This strong effect of collisions on radial electric field dynamics, appearing through a competition between generation and damping, affects in turn through zonal flow shearing the turbulent transport levels, as studied in this paper.

In order to address issues related to collisional turbulent transport with a Particle-in-Cell (PIC) code such as ORB5 [6], the first requirement is to ensure long and relevant simulations despite the numerical noise intrinsic to the PIC method and even enhanced over time by the numerical treatment of collisions. The code ORB5 has proven to enable long, statistically converged collisionless simulations by using a small artificial decay of the weights [7]. The latter noise control scheme is however unpractical for carrying out collisional simulations, since the required numerical decay rate which needs to be chosen for the approach to be effective is typically of the order of the ion-ion collision frequency and may thus significantly interfere with the corresponding physical effects. The control of numerical noise in presence of collisions is thus handled by making use of the so-called coarse-graining procedure, first proposed in [8] and further simplified in [9]. Some details related to the implementation of the coarse graining algorithm in ORB5 are given in this paper.

Another requirement for the code is to feature a robust and thoroughly tested collision operator. The self-collision operators in ORB5 are linearized Landau operators conserving locally the first three velocity moments (density, parallel momentum, kinetic energy) and whose discretization is presented in detail in [10]. Several neoclassical benchmarks against other codes and analytical predictions have been performed. In this paper, we also address the question of whether a simple Lorentz operator for ion-ion collisions used in other codes [11] is sufficient for turbulence studies compared to a more accurate Landau self-collision operator.

Studies of collisional ITG turbulence using gyrokinetic simulations have already been performed in the past, making use of either Lagrangian (PIC) [12] or Semi-Lagrangian [13] methods. Both in [12] and [13], the damping of zonal flows by collisions is found to increase the turbulent heat diffusivity, at all values of the gradients considered. An Eulerian approach combined with a simplified Krook operator for ion-ion collisions provides the same trend, however less pronounced [14]. Turbulence studies in the frame of a Z-pinch configuration lead again to a transport enhancement due to collisions [15]. This general conclusion is confirmed by ORB5 results. In this paper, we systematically analyze the mechanisms of neoclassical (purely collisional) and turbulent transport. To this end, in a first phase of the simulation a neoclassical equilibrium is established by keeping only axisymmetric ($n = 0$) Fourier modes. In a second phase, turbulence can evolve freely by considering all toroidal Fourier modes ($n = 0$ & $n \neq 0$). The main finding of our work is that collisional effects are not simply additive to turbulent transport: heat transport in the presence of both turbulence and collisions is larger than the sum of collisionless turbulent transport and neoclassical transport. The softening of the Dimits shift region obtained in [12] is as well observed in ORB5 simulations and is further characterized in this work. Like the previous results mentioned above, the electrons are assumed adiabatic and therefore collisionless in this paper. Considering the dynamics of kinetic electrons along with the related electron collisionality may lead to different conclusions concerning the effects of collisions on turbulence in certain regimes [16], mainly due to the reduction of microinstability drive by electron collisions.

The paper is organized as follows: Sec. II presents briefly the simulation model and the numerical method, as well as the parameters of the specific considered physical system. Sec. III explains the noise control procedure applied in collisional ORB5 and shows some related

tests. Sec. IV shows some results related to collisional Rosenbluth-Hinton tests which emphasize the difference in zonal flow physics between collisionless and collisional systems. Sec. V addresses the competition between the neoclassical electric field generation and the zonal flow damping by collisions in turbulent simulations starting from a neoclassical equilibrium, and emphasizes the resultant effects on transport for different temperature gradients. Sec. VI considers the relevance of the simple Lorentz operator for ion-ion collisions in the frame of turbulent studies. Conclusions are drawn in Sec. VII. Finally, the effect of the potential energy flux on the heat transport is discussed in Appendix A.

II. SIMULATION MODEL AND NUMERICAL METHODS

A. The gyrokinetic equation

Simulations are performed with the global gyrokinetic code ORB5 [6]. Electrons are considered here in the limit of the adiabatic approximation as one is interested in the purely ITG regime. The collisional model of ORB5 is described in detail in Ref. [10]. It solves the gyrokinetic equation for the gyro-averaged ion distribution function $f(\vec{R}, v_{||}, \mu, t)$, where $\vec{R}$ is the gyrocenter position, $v_{||}$ the parallel velocity and $\mu = mv_{\perp}^2/B$ the magnetic moment. The operator $\hat{C}$ representing ion-ion collisions is a Landau operator, linearized with respect to a local Maxwellian distribution f_{LM}:

$$\hat{C}(\delta f_{LM}) = C[f_{LM}, \delta f_{LM}] + C[\delta f_{LM}, f_{LM}], \tag{1}$$

where $\delta f_{LM} = f - f_{LM}$ represents the deviation of the full distribution f with respect to f_{LM}. The first term on the right hand side represents collisions of δf_{LM} on the background f_{LM} and the second term represents the background reaction (collisions of f_{LM} on δf_{LM}) ensuring the local conservation of density, parallel momentum and kinetic energy. The background reaction term is in fact approximated and of the form [17], [8]:

$$\frac{C[\delta f_{LM}, f_{LM}]}{f_{LM}} \simeq \mathcal{B}(\delta f_{LM}) = \frac{1}{n_0}\left\{6\sqrt{\pi}H(\mathsf{v})\frac{\delta \mathcal{P}_{||} v_{||}}{v_{th}^2} + \sqrt{\pi}\ G(\mathsf{v})\frac{\delta \mathcal{E}}{v_{th}^2}\right\}, \tag{2}$$

where n_0 is the background density, $v_{th} = \sqrt{T/m}$ is the thermal velocity, and $\mathsf{v} = v/v_{th}$. $H(\mathsf{v})$ and $G(\mathsf{v})$ are defined in [10] and related to the Rosenbluth potentials relatively to a

Maxwellian background. $\delta\mathcal{P}_{||}$ and $\delta\mathcal{E}$ are respectively the changes in the parallel momentum and the kinetic energy of the fluctuation distribution due to $C[f_{LM}, \delta f_{LM}]$:

$$\delta\mathcal{P}_{||}(\delta f_{LM}, \vec{x}) = -\int C[f_{LM}, \delta f_{LM}] v_{||} \mathrm{d}^3 v, \tag{3}$$

$$\delta\mathcal{E}(\delta f_{LM}, \vec{x}) = -\int C[f_{LM}, \delta f_{LM}] v^2 \mathrm{d}^3 v. \tag{4}$$

The form (2) ensures the same symmetry properties as the exact background reaction term and associated properties (H-theorem, stationary states). A heat source S_H is also considered, such that the gyrokinetic equation reads:

$$\frac{D}{Dt} f = -\hat{C}(\delta f_{LM}) + S_H, \tag{5}$$

where D/Dt is the collisionless gyrokinetic operator:

$$\frac{D}{Dt} = \frac{\partial}{\partial t} + \frac{\mathrm{d}\vec{R}}{\mathrm{d}t} \cdot \frac{\partial}{\partial \vec{R}} + \frac{\mathrm{d}v_{||}}{\mathrm{d}t} \frac{\partial}{\partial v_{||}}. \tag{6}$$

The gyrokinetic equations of motion for the gyrocenter variables, derived by Hahm [18], are given by:

$$\frac{\mathrm{d}\vec{R}}{\mathrm{dt}} = \vec{v}_G = v_{||}\hat{b} + \underbrace{\vec{v}_{\nabla B} + \vec{v}_c + \vec{v}_{E\times B}}_{\vec{v}_d}, \tag{7}$$

$$\frac{\mathrm{d}v_{||}}{\mathrm{dt}} = \frac{1}{m v_{||}} \vec{v}_G \cdot (q\vec{E} - \mu\vec{\nabla}B), \tag{8}$$

$$\frac{\mathrm{d}\mu}{\mathrm{dt}} = 0, \tag{9}$$

which are valid for small fluctuation levels. Here $\hat{b} = \vec{B}/B$ is the unitary vector along $\vec{B}$, $\vec{v}_G$ is the guiding center velocity, $\vec{v}_{\nabla B}$ is the ∇B drift velocity, $\vec{v}_c$ is the curvature drift velocity, $\vec{v}_{E\times B}$ is the $\vec{E} \times \vec{B}$ drift velocity and $\vec{E}$ is the gyro-averaged electric field deriving from the electrostatic potential ϕ. For more details, the reader is referred to Ref. [6].

B. δf Particle-In-Cell discretization

ORB5 uses the low noise δf PIC method, requiring the introduction of N numerical particles, called markers, for sampling the fluctuation distribution f. The distribution f is split into

a background distribution f_0 and a perturbed part $\delta f = f - f_0$. Introducing two weights $w_r(t)$ and $p_r(t)$ for the marker r, the fluctuation distribution δf and associated background distribution f_0 respectively read:

$$\delta f(\vec{R}, v_{||}, \mu, t) = \sum_{r=1}^{N} \frac{m}{B_{||}^*} w_r(t) \delta[\vec{R} - \vec{R}_r(t)] \delta[v_{||} - v_{||,r}(t)] \delta[\mu - \mu_r(t)], \tag{10}$$

$$f_0(\vec{R}, v_{||}, \mu, t) = \sum_{r=1}^{N} \frac{m}{B_{||}^*} p_r(t) \delta[\vec{R} - \vec{R}_r(t)] \delta[v_{||} - v_{||,r}(t)] \delta[\mu - \mu_r(t)], \tag{11}$$

where $B_{||}^* = B + m v_{||} (\vec{\nabla} \times \hat{b}) \cdot \hat{b}/q$ and r is an indice for labelling the N markers. δ stands here for the Dirac function. The gyrokinetic equation is solved through a time splitting approach, considering successively separately the time stepping of the collisionless dynamics, the collisional dynamics and the source term S_H.

1. *Collisionless stepping*

For solving the collisionless part of the dynamics, the background f_0 is chosen as a so-called canonical Maxwellian $f_{CM}(\hat{\Psi}, \mathcal{E})$ [19]:

$$f_{CM}(\hat{\Psi}, \mathcal{E}) = \frac{n_0(\hat{\Psi})}{[2\pi T_0(\hat{\Psi})/m]^{3/2}} \exp\left[-\frac{\mathcal{E}}{T_0(\hat{\Psi})}\right], \tag{12}$$

where the radial coordinate $\hat{\Psi}$ is the corrected toroidal canonical momentum and reads:

$$\hat{\Psi} = \Psi_0 + \text{corr} = \Psi_0 - \text{sign}(v_{||}) \frac{m}{q} R_0 \sqrt{\frac{2}{m}(\mathcal{E} - \mu B_0)}\, \mathcal{H}(\mathcal{E} - \mu B_0), \tag{13}$$

with $\mathcal{H}$ the Heaviside function, $\mathcal{E} = mv^2/2 = mv_{||}^2/2 + \mu B$ the kinetic energy and B_0 the magnetic field at the magnetic axis. The correction in $\hat{\Psi}$ to the toroidal canonical momentum $\Psi_0 = \Psi + mF(\Psi)v_{||}/qB$, where $F(\Psi) = RB_\varphi$, is nearly zero for trapped particles and of opposite sign for forward and backward passing particles. $\hat{\Psi}$, being clearly a function of constants of motion of the unperturbed system, is itself a constant of motion of the unperturbed system and approximates the average of Ψ over the guiding center trajectory [19]. f_{CM} is thus a function of the constants of the unperturbed motion, $(\hat{\Psi}, \mathcal{E}, \mu)$, and is therefore solution of the stationary, collisionless gyrokinetic equation in absence of perturbations. Due to the remaining velocity dependence of $\hat{\Psi}$, $n_0(\hat{\Psi})$ and $T_0(\hat{\Psi})$, although close, slightly

differ from the actual density and temperature associated to f_{CM} due to finite banana width corrections. Evolving the collisionless part of the gyrokinetic equation is thus performed by integrating numerically in time Eqs. (7)-(9) to obtain the collisionless marker trajectories $z_r(t) = [\vec{R}_r(t), v_{||,r}(t), \mu_t(t)]$ together with weight equations $\mathrm{d}w_r/\mathrm{d}t$ and $\mathrm{d}p_r/\mathrm{d}t$, detailed in [10] and written as follows:

$$\frac{\mathrm{d}}{\mathrm{d}t} w_r(t) \;=\; -p_r(t)\; \frac{1}{f_{CM}} \frac{D}{Dt} f_{CM}\bigg|_{[z_r(t),t]}, \tag{14}$$

$$\frac{\mathrm{d}}{\mathrm{d}t} p_r(t) \;=\; p_r(t)\; \frac{1}{f_{CM}} \frac{D}{Dt} f_{CM}\bigg|_{[z_r(t),t]}. \tag{15}$$

The collisionless dynamics is handled through the so-called direct-δf method [20], taking advantage of the fact that the total distribution f is conserved along collisionless trajectories. The weight equations for collisionless dynamics can in fact be integrated analytically:

$$\frac{\mathrm{d}}{\mathrm{d}t}(w_r(t) + p_r(t)) \;=\; 0 \Longrightarrow w_r + p_r = \text{const.}, \tag{16}$$

$$\frac{\mathrm{d}}{\mathrm{d}t} \ln \frac{p_r}{f_{CM}|_{z_r}} \;=\; 0 \Longrightarrow \frac{p_r}{f_{CM}|_{z_r}} = \text{const.}, \tag{17}$$

Eq. (16) resulting from adding relations (14) & (15) and Eq. (17) obtained directly from integration of Eq. (15). Let us suppose a marker r going from position $z_r(t) = [\vec{R}_r(t), v_{||,r}(t), \mu_r(t)]$ to position $z_r(t+\Delta t) = [\vec{R}_r(t+\Delta t), v_{||,r}(t+\Delta t), \mu_r(t+\Delta t)]$ during a collisionless time step $t \to t + \Delta t$. Making use of Eqs. (16)-(17), the new weights are given by:

$$p_r(t+\Delta t) \;=\; p_r(t) \frac{f_{CM}|_{z_r(t+\Delta t)}}{f_{CM}|_{z_r(t)}}, \tag{18}$$

$$w_r(t+\Delta t) \;=\; w_r(t) + p_r(t) - p_r(t+\Delta t). \tag{19}$$

This scheme allows to avoid evaluating explicitly unpractical terms such as $\mathrm{d}\hat{\Psi}/\mathrm{d}t$, appearing through Df_{CM}/Dt in equations (14) & (15) for the time evolution of the weights.

2. Collisional stepping

For the purely collisional part of the time splitting approach, the background f_0 is chosen as a local Maxwellian $f_{LM}(\Psi, \mathcal{E})$:

$$f_{LM}(\Psi, \mathcal{E}) = \frac{n_0(\Psi)}{[2\pi T_0(\Psi)/m]^{3/2}} \exp\left[-\frac{\mathcal{E}}{T_0(\Psi)}\right], \tag{20}$$

where Ψ is the poloidal magnetic flux and $n_0(\Psi)$ and $T_0(\Psi)$ the background density and temperature profiles respectively. The transition between the local background f_{LM} representation and the canonical background f_{CM} representation, used for solving the collisional and the collisionless dynamics respectively, is provided by the background switching scheme described in detail in [10]. Collisions of δf_{LM} on f_{LM}, so-called test particle collisions represented by $C[f_{LM}, \delta f_{LM}]$, are modelled through random kicks for markers in velocity space, according to the Langevin approach, while collisions of f_{LM} on δf_{LM} appear through the following collisional weight equations:

$$\frac{\mathrm{d}}{\mathrm{d}t} w_r(t) \;=\; -p_r(t)\, \frac{C[\delta f_{LM}, f_{LM}]}{f_{LM}}\bigg|_{[z_r(t),t]}, \tag{21}$$

$$\frac{\mathrm{d}}{\mathrm{d}t} p_r(t) \;=\; 0. \tag{22}$$

The background reaction implementation ensures the conservation of density, parallel momentum and kinetic energy to round-off precision [21]. More details about the numerical methods are given in Ref. [10]. In particular, the binning of markers in configuration space for estimating the fields $\delta\mathcal{P}_{||}(\vec{R}, t)$ and $\delta\mathcal{E}(\vec{R}, t)$, representing the local variations of parallel momentum and kinetic energy from test particle collisions and appearing in the background reaction of the collision operator (2), is now performed in 3 dimensions as the turbulence structures vary along all configuration space dimensions, while a binning in the 2 dimension poloidal plane is sufficient for the axisymmetric neoclassical runs described in [10]. The binning related to collisions is field-aligned, in order to take advantage of the turbulence structure, and equivalent to the binning for the coarse graining in configuration space described in Section III.

The collisionality is defined through the normalized ν^* parameter, which is the ratio between the detrapping collision frequency and the bounce frequency:

$$\nu_i^* = \frac{R_0 q_s}{\tau_{ii} v_{thi} \epsilon^{3/2}}, \text{ with } \tau_{ii} = \frac{6\sqrt{\pi}}{\nu_{ii}}, \tag{23}$$

where ν_{ii} is the thermal self-collision frequency for ions:

$$\nu_{ii} = \frac{n_{i0} q_i^4 \ln \Lambda}{2\pi \epsilon_0^2 m_i^2 v_{thi}^3}. \tag{24}$$

The Coulomb logarithm $\ln \Lambda$ is assumed to be constant over the whole plasma and typically chosen $\ln \Lambda = 18$. Except for the Coulomb logarithm, the radial dependance of the collisionality, through density and temperature profiles, is accounted for. The notation ν_0^* is introduced and stands for the collisionality parameter at the reference surface.

3. Heat sources

The global heat source S_H is aimed at maintaining a roughly constant temperature profile despite the outward heat flux. It takes the form [7]:

$$S_H = -\gamma_H \left(\widetilde{\delta f}_{CM}(\Psi, \mathcal{E}, t) - \widetilde{f_{CM}}(\Psi, \mathcal{E}, t) \frac{\int d\mathcal{E}\ \widetilde{\delta f}_{CM}(\Psi, \mathcal{E}, t)}{\int d\mathcal{E}\ \widetilde{f_{CM}}(\Psi, \mathcal{E}, t)} \right), \tag{25}$$

where $\widetilde{\ }$ stands for the distribution reconstruction operator in the $(\Psi, \mathcal{E})$ space, which requires a binning in the $(\Psi, \mathcal{E})$ space. For any function A of the gyrocenter variables $(\Psi, \theta^*, \varphi, \mathcal{E}, \xi)$, where θ^* is the straight-field line poloidal angle, φ the toroidal angle and $\xi = v_{||}/v$ the pitch angle, the operator $\widetilde{\ }$ reads:

$$\widetilde{A}(\Psi, \mathcal{E}, t) = \frac{\int \mathrm{d}\theta^* \mathrm{d}\varphi \mathrm{d}\xi\ J_{\theta^* \Psi \varphi} A(\Psi, \theta^*, \varphi, \mathcal{E}, \xi)}{2 \int \mathrm{d}\theta^* \mathrm{d}\varphi\ J_{\theta^* \Psi \varphi}}, \tag{26}$$

$J_{\theta^* \Psi \varphi}$ being the Jacobian function. The heating rate γ_H is typically chosen as 10% of the linear growth rate of the most unstable ITG mode. Note that the heat source term (25) is particle and momentum conserving, and is constant on a given flux-surface. Eq. (25) is integrated separately from other dynamics in the frame of the time splitting approach.

C. Quasi-neutrality equation

The electrostatic approximation is assumed in our model. The electrons are considered adiabatic and enter the model through the quasi-neutrality equation:

$$\frac{e n_e(\Psi)}{T_e(\Psi)} [\phi(\vec{x}, t) - \langle \phi \rangle(\Psi, t)] - \nabla_\perp \cdot \left(\frac{n_{i0}(\Psi)}{B \Omega_i} \nabla_\perp \phi \right) = \bar{\delta n}_i(\vec{x}, t), \tag{27}$$

where ϕ is the electrostatic potential, $T_e(\Psi)$ is the electron temperature profile, Ω_i the ion cyclotron frequency, e is the elementary charge and $\langle\rangle$ stands for the flux surface average operator. $\bar{\delta n_i}(\vec{x})$ is the perturbed ion gyrodensity, computed as follows:

$$\bar{\delta n_i}(\vec{x},t) = \int \frac{B_{||}^*}{m}\, \mathrm{d}^3R\, \mathrm{d}v_{||}\, \mathrm{d}\mu\, \delta f_{CM,i}(\vec{R}, v_{||}, \mu, t)\delta(\vec{R} + \vec{\rho}_{Li} - \vec{x}), \tag{28}$$

where $\delta f_{CM,i} = f_i - f_{CM,i}$ and $\vec{\rho}_{Li}$ is the ion Larmor vector. It is assumed that the ion background gyrodensity, defined as:

$$\bar{n}_{i0}(\vec{x}) = \int \frac{B_{||}^*}{m}\, \mathrm{d}^3R\, \mathrm{d}v_{||}\, \mathrm{d}\mu\, f_{CM,i}(\vec{R}, v_{||}, \mu)\delta(\vec{R} + \vec{\rho}_{Li} - \vec{x}), \tag{29}$$

is equal to the ion background density $n_{i0}(\hat{\Psi})$ associated to the background distribution $f_{CM,i}$. One assumes furthermore that the background densities of electrons and ions verify quasi-neutrality, i.e. $Zn_{i0} = n_{e0}$, where Z is the ionization degree. The last term on the left hand side of Eq. (27) is the linearized polarization drift, derived considering the long wavelength approximation ($k_\perp \rho_{Li} \ll 1$, where ρ_{Li} is the ion Larmor radius). Under this assumption, the polarization drift term, which in general is an integral operator, reduces to a differential operator (Poisson-like equation) and is valid only up to second order in $k_\perp \rho_{Li}$. Note that the considered adiabatic electron response is also linearized, having furthermore invoked small amplitude fluctuations, so that $|e(\phi - \langle\phi\rangle)/T_e| \ll 1$. The details of the numerical implementation of the quasineutrality equation solver are given in [6] and [22].

D. Transport diagnostics

We define respectively the gyrocenter particle flux Γ, the kinetic energy flux Q_{kin}, the potential energy flux Q_{pot} and the heat flux q_H as follows:

$$\Gamma = \left\langle \frac{\vec{\nabla}\Psi}{|\vec{\nabla}\Psi|} \cdot \int \mathrm{d}^3 v f \frac{\mathrm{d}\vec{R}}{\mathrm{d}t} \right\rangle_S = \left\langle \frac{1}{|\vec{\nabla}\Psi|} \int \mathrm{d}^3 v f \frac{\mathrm{d}\Psi}{\mathrm{d}t} \right\rangle_S , \tag{30}$$

$$Q_{kin} = \left\langle \frac{1}{|\vec{\nabla}\Psi|} \int \mathrm{d}^3 v \frac{m}{2} v^2 f \frac{\mathrm{d}\Psi}{\mathrm{d}t} \right\rangle_S , \tag{31}$$

$$Q_{pot} = \left\langle \frac{1}{|\vec{\nabla}\Psi|} \int \mathrm{d}^3 v \; q\phi f \frac{\mathrm{d}\Psi}{\mathrm{d}t} \right\rangle_S , \tag{32}$$

$$q_H = \left\langle \frac{1}{|\vec{\nabla}\Psi|} \int \mathrm{d}^3 v \left[\frac{m}{2}(v^2 - 5v_{th}^2) + q\phi \right] f \frac{\mathrm{d}\Psi}{\mathrm{d}t} \right\rangle_S , \tag{33}$$

where $\mathrm{d}\Psi/\mathrm{d}t = \vec{\nabla}\Psi \cdot \mathrm{d}\vec{R}/\mathrm{d}t$ and $\langle \mathcal{A} \rangle_S = (1/S) \int_S \mathcal{A} \; \mathrm{d}\sigma$ is defined as the poloidal flux surface average of a quantity $\mathcal{A}$, S being the surface value. In practice, to ensure sufficient statistical accuracy from the PIC approach, surface averages are replaced by volume averages using the relation $\langle \mathcal{A} \rangle_S = \langle |\vec{\nabla}\Psi| \mathcal{A} \rangle_{\Delta V} / \langle |\vec{\nabla}\Psi| \rangle_{\Delta V}$, where $\langle \mathcal{A} \rangle_{\Delta V} = \int_{\Delta V} \mathcal{A} \; \mathrm{d}^3 x / \Delta V$ stands for the volume average over the small volume ΔV enclosed between two neighboring magnetic surfaces Ψ and $\Psi + \Delta\Psi$. The heat flux q_H can be written as:

$$q_H = Q_{kin} + Q_{pot} - \frac{5}{2} T \; \Gamma. \tag{34}$$

Note that the presented simulations take into account the potential energy flux for a relevant computation of the heat diffusivity [23]. For diagnostic purposes, the effective heat diffusivity is estimated using the following relation: $\chi_H = q_H/(n|\nabla T|)$. Let us emphasize that this relation is based on the approximation of neglecting the off-diagonal elements of the transport matrix as in general, density gradients also contribute to the heat flux. Diffusivities are usually normalized with respect to the Gyro-Bohm (GB) units: $\chi_{GB} = c_s \rho_s^2 / a$, where $c_s = \sqrt{ZT_e/m_i}$ is the sound speed and the sound Larmor radius is defined as $\rho_s = c_s/\Omega_i$, with T_e taken at the reference radial position $r/a = 0.5$ and the cyclotron frequency $\Omega_i = ZeB/m_i$ evaluated using the magnetic field on axis.

The so-called neoclassical fluxes are obtained from the contributions $\delta f_{CM} \cdot \mathrm{d}\Psi/\mathrm{d}t|_0$ and $f_{CM} \cdot \mathrm{d}\Psi/\mathrm{d}t|_{E\times B}$ in Eqs. (30)-(33), while the so-called turbulent fluxes, the usual fluxes computed in collisionless gyrokinetic codes, are provided by the contribution $\delta f_{CM} \cdot \mathrm{d}\Psi/\mathrm{d}t|_{E\times B}$ to $f \cdot \mathrm{d}\Psi/\mathrm{d}t$. Here one has introduced the $\vec{E} \times \vec{B}$ drift contribution to the radial velocity $\mathrm{d}\Psi/\mathrm{d}t|_{E\times B} = \vec{\nabla}\Psi \cdot \vec{v}_{E\times B}$ and the magnetic drift contribution to the radial velocity $\mathrm{d}\Psi/\mathrm{d}t|_0 =$

$\vec{\nabla}\Psi \cdot (\vec{v}_{\nabla B} + \vec{v}_c)$. The fluxes associated to $f_{CM} \cdot \mathrm{d}\Psi/\mathrm{d}t|_0$ do vanish as f_{CM} represents a stationary state of the collisionless system.

E. Magnetic Equilibrium

The considered *adhoc* equilibrium [24] consists of toroidal, axisymmetric, nested magnetic surfaces with circular, concentric, poloidal cross-sections. In this case, the axisymmetric magnetic field is given by $\vec{B} = \vec{\nabla}\Psi \times \vec{\nabla}\varphi + F(\Psi)\vec{\nabla}\varphi$, assuming $\Psi = \Psi(r)$ with $\mathrm{d}\Psi/\mathrm{d}r = rB_0/\bar{q}(r)$, as well as $F = RB_\varphi = R_0B_0$, so that:

$$\vec{B} = \frac{B_0R_0}{R}\left(\hat{e}_\varphi + \frac{r}{R_0\bar{q}(r)}\hat{e}_\theta\right), \tag{35}$$

where R is the major radius, r the local minor radius, φ the toroidal angle, θ the poloidal angle and $\hat{e}_\varphi$, $\hat{e}_\theta$ the unit vectors in the toroidal and poloidal directions, respectively. The transformation between the toroidal variables (r, φ, θ) and the cylindrical variables (R, φ, z) is provided by $R = R_0 + r\cos\theta$ and $z = r\sin\theta$. Furthermore, B_0 and R_0 stand for the magnetic field amplitude and major radius on the magnetic axis ($r = 0$). The $\bar{q}$ profile is chosen quadratic:

$$\bar{q}(r) = \bar{q}_0 + \bar{q}_1\frac{r^2}{a^2}, \tag{36}$$

which is related to the safety factor profile $q_s(r)$ by the following relation:

$$\bar{q}(r) = \sqrt{1-\epsilon^2}\; q_s(r), \tag{37}$$

where $\epsilon = r/R_0$ is the local inverse aspect ratio. The values $\bar{q}_0 = 0.854$ and $\bar{q}_1 = 2.184$ have been chosen such that $\bar{q}(r/a = 0.5) = 1.4$ and the magnetic shear $(r/\bar{q})\mathrm{d}\bar{q}/\mathrm{d}r|_{r=0.5a} = \hat{s}(r/a = 0.5) = 0.8$.

F. Physical parameters

For the simulation results presented in this paper, the physical parameters are inspired by the DIII-D shot underlying the CYCLONE test case [25] and similar to the parameters considered in [12] and [13]. The considered aspect ratio is $a/R_0 = 0.36$, where a is the global

minor radius. Choosing $T_e(r) = T_i(r)$ and Deuterium as the ion species, the size of the plasma is set at $a/\rho_s = 180$, where ρ_s is the sound Larmor radius defined in Sec. II D. Let $\mathcal{A}$ stand for either the temperature T or density n of a given species. Profiles are defined with respect to the coordinate r, with a flat logarithmic gradient:

$$\frac{\mathrm{d}\ln\mathcal{A}}{\mathrm{d}(r/a)} = -\frac{\kappa_{\mathcal{A}}}{2}\left[\tanh\left(\frac{r-(r_0-\Delta_{\mathcal{A}})}{\Delta_r}\right) - \tanh\left(\frac{r-(r_0+\Delta_{\mathcal{A}})}{\Delta_r}\right)\right], \tag{38}$$

where the values $r_0 = 0.5a$ for the center of the gradient profile and $\Delta_r = 0.04a$ for the width of the ramps have been chosen. Two actual gradient profile widths are considered: a narrow one with $\Delta_{\mathcal{A}} = 0.15a$ and a wide one with $\Delta_{\mathcal{A}} = 0.3a$. For the density profile $\kappa_n = 0.789$ such that $R_0/L_n = R_0\kappa_n/a = 2.2$ at $r = r_0$. Two temperature gradients, namely $R_0/L_{T_0} = 5.3$ and $R_0/L_{T_0} = 6.9$, are studied in the next sections, corresponding to $\kappa_T = 1.908$ and $\kappa_T = 2.484$ respectively. The physical collisionality (see Eq. (23)) at $r = r_0$ for the CYCLONE case parameters is $\nu^*_{\mathrm{phys}} \simeq 0.045$. Collisionalities larger than the physical one, ranging from 2 ν^*_{phys} up to 10 ν^*_{phys}, are studied in this paper, in order to emphasize the effects of collisions on the system.

G. Numerical parameters

The grid in configuration space chosen for solving the Poisson equation in this system is $N_r \times N_\theta \times N_\varphi = 128 \times 512 \times 256$, where N_r, N_θ and N_φ are the number of grid points in the radial, poloidal and toroidal direction respectively. For the turbulent simulations, only every second toroidal Fourier mode of the solution given by Eq.(27) is retained, namely $n = 0, 2, 4, \ldots, 56$, corresponding in real space to restricting the system to a toroidal wedge of half the full system. A time step of $\Delta t = 0.22[a/c_s]$ is chosen. For the CYCLONE case described above, the number of markers ranges typically from $\sim 100 \times 10^6$ for collisionless runs up to 500×10^6 for collisional runs.

III. CONTROLLING NUMERICAL SAMPLING NOISE IN COLLISIONAL SIMULATIONS

A. Fourier filtering and signal-to-noise ratio estimate

Numerical sampling noise is diagnosed in ORB5 by examining the spatially averaged squared density fluctuation amplitude in non-resonant, high-$k_{||}$ turbulent modes, which are physically supposed to be strongly Landau damped. These latter modes are thus at the limit or even beyond the gyrokinetic ordering, and only arise due to sampling errors [26]. Here, $k_{||} \simeq (nq_s - m)/Rq_s$ is the component of the wave vector of a given poloidal-toroidal Fourier mode (m, n) parallel to the magnetic field. Let us point out that the Fourier modes are computed using a straight-field-line poloidal angle θ^*. Invoking the fact that microturbulence is essentially aligned along the magnetic field lines, the charge density is Fourier-filtered, i.e. the quasi-neutrality solver retains only the Fourier modes (n, m) which, at a given radial position Ψ, are such that $|nq_s(\Psi) - m| \leqslant \Delta m$, where $\Delta m = 5$ is typically used. Due to the validity range of the long wavelength approximation, the upper boundary for the toroidal Fourier modes n is typically chosen such that $k_\perp \rho_{Li} \simeq nq_s(r_0)\rho_{Li}/r_0 \leqslant 0.8$. In order to define a signal-to-noise ratio, the following definitions are introduced: the signal is estimated by the energy in the modes inside a certain Fourier filter $\mathcal{F}$ (low-$k_{||}$ modes), while the noise is estimated by the modes outside the Fourier filter (high-$k_{||}$ modes):

$$\text{signal} = \frac{1/a \int_0^a dr \sum_{(n,m)\in\mathcal{F}} |\delta n^{(n,m)}(r)|^2}{\sum_{(n,m)\in\mathcal{F}}}, \qquad \text{noise} = \frac{1/a \int_0^a dr \sum_{(n,m)\notin\mathcal{F}} |\delta n^{(n,m)}(r)|^2}{\sum_{(n,m)\notin\mathcal{F}}}, \tag{39}$$

where the energy-like estimates are computed on the basis of the density fluctuations. The Fourier components outside the filter $\mathcal{F}$ are removed from the density fluctuations before computing the electrostatic field. This is the basic noise-control procedure. If the noise becomes large compared to the physical signal, the simulations become irrelevant and are not further carried out. The critical level of the signal/noise ratio (SNR) which is considered to provide relevant results was empirically found to be SNR $\simeq 10$. In this paper we describe an additional noise-control procedure in ORB5 for collisional runs, the so-called coarse-graining method, first proposed in [8] and further simplified in [9].

B. Coarse-graining

The coarse graining procedure involves 1) the binning of the markers in the whole gyrokinetic phase space, i.e. a 5D binning, at a given time step and 2) the smoothing of the marker weights within a same bin.

1. Binning

Let us emphasize the critical choice of the bin size. The bins indeed need to be as large as possible to ensure the best statistics, but not larger than any physical scale of interest. Indeed, the coarse graining procedure in fact provides numerical diffusion of fluctuation structures in phase space with scales below the binning grid considered to be poorly resolved. Let us define the normalized kinetic energy $\mathbf{E} = v^2/2T(r)$ and the pitch angle $\xi = v_{||}/v$. Note that the energy dimension depends on the radial coordinate through the temperature profile $T(r)$. A uniform grid in θ^* is first built, leading to N_{θ^*} bins. Let us write $\theta_0^*(\theta^*)$ the function giving the position of the bin center θ_0^* corresponding to θ^*:

$$\theta_0^*(\theta^*) = \left[\text{FLOOR}\left(\frac{\theta^* + \pi}{\Delta\theta^*}\right) + \frac{1}{2}\right]\Delta\theta^* - \pi, \tag{40}$$

where $\theta^* \in [-\pi; \pi[$ and $\Delta\theta^* = 2\pi/N_{\theta^*}$ is the width of the bins along θ^*. FLOOR(x) stands for the largest integer which is smaller or equal to x. We define a new field-aligned coordinate z:

$$z = \varphi - q_s(s)[\theta^* - \theta_0^*(\theta^*)]. \tag{41}$$

where q_s is the safety factor and $s = \sqrt{\Psi/\Psi_{\text{edge}}}$ a normalized radial coordinate. Note that this field-aligned coordinate enables to use the largest possible bins in the θ^* direction, which now parametrizes the position along the field line. Indeed in the coordinates (s, θ^*, z) the dependance with respect to θ^* of a field-aligned fluctuation quantity represents the slowly varying envelope along the magnetic line. The fast phase variation transverse to the magnetic field is represented by both s and z. The binning is then defined as a block-structured Cartesian grid in the new set of variables $(s, \theta^*, z, \mathbf{E}, \xi)$. The number of bins in the θ^* direction is proportional to the radial coordinate s ($s\Delta\theta^* \sim$ const.) in order to ensure good statistics, including near the magnetic axis, which is the center of the polar-like

coordinates (s, θ^*). Figure 1 shows how the binning follows the field lines in the (θ^*, φ) plane, as well as the bin structure in the (θ^*, z) plane and in the (θ^*, s) plane.

2. Smoothing

Let us write α the general index identifiying a 5D bin. Considering the bin α, we define the averaged w-weight and p-weight for the markers with index r present in the bin α at a given time:

$$\bar{w}_\alpha(t) \;=\; \frac{1}{N_\alpha} \sum_{r \in \alpha} w_r(t), \tag{42}$$

$$\bar{p}_\alpha(t) \;=\; \frac{1}{N_\alpha} \sum_{r \in \alpha} p_r(t), \tag{43}$$

where N_a is the number of markers in the bin α. Let us consider a marker r in a bin α. Introducing the relaxation rates γ_w and γ_p, the modification brought to both weights of the marker r after a coarse graining procedure is:

$$\Delta w_r \;=\; \mathcal{N} \Delta t \cdot \gamma_w \cdot (\bar{w}_\alpha - w_r)\,, \tag{44}$$

$$\Delta p_r \;=\; \mathcal{N} \Delta t \cdot \gamma_p \cdot (\bar{p}_\alpha - p_r)\,, \tag{45}$$

where $\mathcal{N}$ is the number of time steps of length Δt between which coarse graining is performed. The typical parameters for the simulations presented in this paper are $\mathcal{N} = 10$, $\gamma_w = 0.45[c_s/a]$ and $\gamma_p = 0.045[c_s/a]$. The chosen values are specific to given physical quantities, like the growth rate of the instability or the collisionality, and are not universal. The only mandatory requirement is $\mathcal{N}\Delta t \cdot \gamma_w \leqslant 1$. A full relaxation of all weights in a bin to the averaged weight value corresponds to $\mathcal{N}\Delta t \cdot \gamma_w = 1$.

C. Effects on turbulence

The purpose of the coarse-graining is to reduce the numerical noise, by filtering the high-k modes both in configuration and velocity space in case of a collisionless run and/or by reducing the weight spreading in case of a collisional run [8]. The aim of this procedure is to

enable to maintain the signal/noise ratio at a higher level than simulations without coarse graining, while retaining the key physics from the simulation. As already mentioned, the size of the bins needs to be chosen so as to be smaller than any scale length relevant to a correct estimation of the turbulent transport levels. Bin sizes are thus similar to mesh sizes used in grid-based (Eulerian) gyrokinetic codes. Considering the CYCLONE base case described in Sec. II F with $R_0/L_{T_0} = 6.9$ and taking $n_s \times n_{\theta^*} \times n_z \times n_{\mathbf{E}} \times n_\xi = 128 \times 32 \times 128 \times 40 \times 40$ as the binning grid for half of the torus, we first consider a non-heated plasma discretized with 100×10^6 markers. Figure 2 shows that the coarse graining procedure has no significant effect on the growth and non-linear saturation of different ITG modes, $n = 10$ and $n = 44$ corresponding respectively to $k_\perp \rho_{Li} \simeq 0.15$ and $k_\perp \rho_{Li} \simeq 0.68$. The latest result is in accordance with the purpose of the coarse graining procedure, which is to address a purely numerical issue and thus has to leave the physics unchanged. The size of the binning is, as expected, very important: if the bins are too large, significant scales of the turbulence are affected, as the corresponding modes are artificially damped, as one sees in Figure 2 for a number of bins reduced by a factor two in each direction.

Considering the appropriate binning mentioned above, the positive effect of the coarse-graining is clearly illustrated in Figure 3, showing the signal/noise ratio for runs with either 90×10^6 or 180×10^6 markers, the heating operator being turned on. On average, there is less than one marker per bin (~ 0.1 and ~ 0.2 respectively). It has to be noticed from Figure 3 that the coarse-graining procedure is able to stabilize the signal/noise ratio. The simulations for which the noise is not controlled by the coarse-graining method indeed present a decaying signal/noise ratio in the time evolution, finally reaching a level below the threshold of simulation relevance (~ 10). The described coarse-graining procedure allows to carry out relevant, i.e. long enough studies of turbulence in the frame of the δf PIC method.

Let us emphasize again that this noise control method is fully compatible with the physics of collisions [10]. Furthermore, note that the field-aligned coordinates are compatible with the gyrokinetic ordering (small $k_{||}\rho_{Li}$) and are thus the natural choice for representing micro-turbulence. Considering bins aligned along these coordinates enables to take the largest possible bins, essential for ensuring, on average, sufficient statistics within each bin, while avoiding the coarse-graining procedure to smooth out essential physical scale lengths. This

is illustrated by the number of bins considered in configuration space ($128 \times 32 \times 128$ for half of the torus) versus the number of grid points considered in straight field line coordinates for the field solver ($128 \times 512 \times 128$ for half of the torus). It is emphasized that the coarse-graining does not necessarily require more than one marker in each bin at each time step. Such a requirement would naturally compromise any advantage of a PIC method versus an Eulerian approach.

IV. COLLISIONAL ROSENBLUTH-HINTON TESTS

This section points out essential differences between collisionless and collisional behaviour of the zonal flows by showing some results related to the so-called Rosenbluth-Hinton test [5] [27]. The standard parameters given in Sec. II F are considered, except that temperature and density profiles with a peaked shape, as described by Eq. (43) of Ref. [10], are used in this section. An initial distribution perturbation $\delta f_{LM} = (\delta n/n_0)\cos(\pi r/a) f_{LM}$, i.e. radially shaped by a cosine density perturbation, is loaded. The system is then linearly evolved by retaining only the axisymmetric component ($n = 0$ modes) of the electrostatic potential. In collisionless simulations, after relaxation of GAMs oscillations, the residual value of the radial electric field is proportional to the initial amplitude of the perturbation [27], in both cases where profile gradients are or are not considered. In collisional simulations, the situation is fundamentally different: independent of the initial amplitude, the zonal flows dampen as a result of collisions between passing and trapped ions [5] and the radial electric field always relaxes towards the neoclassical equilibrium value, which is non-zero for finite background profile gradients, regardless of the initial electric field amplitude. As expected, the neoclassical equilibrium field does vanish if no gradients are considered. Figures 4 and 5 illustrate these different scenarios by presenting the time evolution of the radial electric field $E_r(t)$ at $r/a = 0.5$, for both zero and non-zero CYCLONE case density and temperature gradients.

V. COLLISIONAL TURBULENT SIMULATIONS STARTED FROM A NEOCLASSICAL EQUILIBRIUM

Simulations have been carried out for collisionalities in the range $\nu^* = 0.09-0.45$, i.e. 2 to 10 times higher than the physical one $\nu^*_{\rm phys} \approx 0.045$. Note that for studying collisional effects, simulations must be carried out over multiple collision times while resolving the shorter time scale of the turbulent fluctuations. Low collisionality is thus numerically challenging due to the large number of time steps as well as the large number of markers required for ensuring a sufficient signal/noise ratio. Collisional simulations are performed with 500×10^6 markers and started from a canonical Maxwellian as the total initial distribution: $f(t=0) = f_{CM}(\hat{\Psi})$. For collisional simulations, a first run with only axisymmetric modes ($n = 0$) is carried out over approximately two collision times τ_{ii}, in order to establish a neoclassical electric field. The simulation is then resumed taking into account both the axisymmetric and the non-axisymmetric modes, thus allowing turbulence to develop and enabling to study the resulting anomalous transport and the interaction between zonal flows and turbulence. The typical time evolution of the neoclassical and turbulent contributions to the kinetic energy flux Q_{kin} (as defined in Sec. II D) , both in the neoclassical and turbulent phase of the simulation, is shown in Figure 6 for the temperature gradient $R_0/L_{T_0} = 6.9$ and collisionality $\nu^*_0 = 4\nu^*_{\rm phys} = 0.18$. The use of the heat source described by Eq. (25) enables to reach a quasi-stationary level of transport by maintaining a constant temperature gradient, in a time-averaged sense.

A. Heat diffusivity: temperature gradient and collisionality effects

In this section, two temperature gradients are first considered, along with a wide non-zero gradient profiles ($\Delta_{\mathcal{A}} = 0.3a$) for carrying out a collisionality scan. The first one, $R_0/L_{T_0} = 5.3$, is above the linear stability threshold, but below the collisionless non-linear stability threshold of ITG turbulence in the considered physical system, i.e. in the so-called Dimits shift region [25]. The second one, $R_0/L_{T_0} = 6.9$, is above the non-linear stability threshold and thus ensures a stronger drive for the turbulence. Figure 7 shows the quasi-stationary total and neoclassical heat diffusivity χ_H at mid-radius with respect to the collisionality. For the gradient under the non-linear stability threshold, $R_0/L_{T_0} = 5.3$, a non-

vanishing turbulent transport illustrating a softening of the Dimits shift region is established through collisions. The turbulent diffusivity is relatively small in this latter case, i.e. of the order of the neoclassical diffusivity at each collisionality ($\chi_H^{\rm tot} = \chi_H^{\rm neo} + \chi_H^{\rm turb} \simeq 2\chi_H^{\rm neo}$). Note that, as expected, there is zero transport at $R_0/L_{T_0} = 5.3$ if the collisions are switched off. For the higher temperature gradient $R_0/L_{T_0} = 6.9$, the increase of the total diffusivity due to collisions is significantly larger than for $R_0/L_{T_0} = 5.3$. For all gradients above the linear gradient threshold, one thus observes:

$$\chi_H^{\rm tot}(\nu^*) > \chi_H^{\rm turb}(\nu^* = 0) + \chi_H^{\rm neo}(\nu^*). \tag{46}$$

In general, the heat transport in the presence of both turbulence and ion-ion collisions is thus larger than the sum of collisionless turbulent and neoclassical transport considered separately. This reflects the complex interplay between collisional effects, zonal flows and turbulence. Figure 8 presents the quasi-stationary diffusivity profiles χ_H for $\nu_0^* = 10\nu_{\rm phys}^* = 0.45$. The neoclassical contribution computed during the turbulent phase is compared to an analytical prediction derived by Chang and Hinton [28], showing a good agreement. While the anomalous transport is of the order of the neoclassical transport in the case of the lower gradient $R_0/L_{T_0} = 5.3$, it becomes clearly dominant for $R_0/L_{T_0} = 6.9$.

As the ion-ion collisions have a marginal influence on the growth rate of the ITG modes in the linear phase of the simulation, it is expected that the effects of collisions on the turbulent transport happen mainly through their damping effect on the zonal flow. The zonal flow is thus a key physical quantity to be studied in order to get insights into the collisional turbulent transport, as it is in the collisionless case. The standard collisionless picture of the interaction between zonal flows and turbulence is the following: above the linear threshold in the ion temperature gradient for the ITG instability, turbulence starts to develop and non-linearly drives zonal modes which in turn tend to quench the turbulence due to the $\vec{E} \times \vec{B}$ shearing rate $\omega_{E\times B}$, given by the following approximate form [29]:

$$\omega_{E\times B} = \frac{r}{q_s B_0} \frac{\mathrm{d}}{\mathrm{d}r} \left(\frac{q_s E_r}{r} \right). \tag{47}$$

The maximum saturation level of zonal flows is determined by a tertiary, Kelvin-Helmoltz (KH) type instability [30], a mechanism transferring energy back from zonal flows to turbulence. If the zonal shearing rate $\omega_{E\times B}$ is strong enough below or at its KH saturation level in

order to quench the turbulence, as it is the case for the temperature gradient $R_0/L_{T_0} = 5.3$, no turbulent transport occurs. On the contrary, if the turbulence is strong enough, as it is the case for the temperature gradient $R_0/L_{T_0} = 6.9$, it is not totally quenched by the saturated zonal flows and some turbulent transport develops. The existence of a tertiary instability threshold setting a saturation level on the zonal flows thus explains the end of the Dimits shift region starting from $R_0/L_{T_0} \simeq 6$, where the turbulence drive becomes too large compared to the saturated zonal flow level and is thus able to produce finite anomalous transport. Figures 9 and 10 show the time evolution of the radial shearing rate profile $\omega_{E\times B}(r)$ for $\nu_0^* = 0.18$, considering $R_0/L_{T_0} = 5.3$ and $R_0/L_{T_0} = 6.9$ respectively. The shearing rate structure and intensity depend naturally on the considered gradient, but in both cases a quasi-stationary state is reached in the end of the simulation.

As predicted in Ref. [5] and as illustrated in Sec. IV, the zonal flows driven by turbulence are shown to be damped by ion-ion collisions. In order to deal with a global shearing rate, we define the radial average operator over the width of the gradients:

$$\langle \cdots \rangle_r = \frac{1}{2\Delta_{\mathcal{A}}} \int_{r_0-\Delta_{\mathcal{A}}}^{r_0+\Delta_{\mathcal{A}}} \cdots \mathrm{d}r. \tag{48}$$

The radial average of the shearing rate absolute value $\langle |\omega_{E\times B}| \rangle_r$ is time averaged over a window of $200[a/c_s]$, moved within the quasi-stationary phase of the simulation in order to get an estimate of the statistical error. For both temperature gradients $R_0/L_{T_0} = 5.3$ (Table I) and $R_0/L_{T_0} = 6.9$ (Table II), the averaged shearing rate $\langle |\omega_{E\times B}| \rangle_{r,t}$ is slightly damped by a finite collisionality but remains of the order of its collisionless level. Moreover, increasing the finite collisionality does not lead to an increase of the damping. The additional drive for zonal flows, coming from the additional turbulence observed in collisional simulations, appears thus to compensate at least partially the damping of turbulence-driven zonal flows by ion-ion collisions.

Table I. Average of the shearing rate absolute value $\langle |\omega_{E\times B}| \rangle_{r,t}$ for $R_0/L_{T_0} = 5.3$.

ν_0^*	0	0.09	0.18	0.3	0.45
$\langle |\omega_{E\times B}| \rangle_{r,t} [10^{-2} c_s/a]$	5.6 ± 0.09	4.9 ± 0.03	4.8 ± 0.03	5.2 ± 0.01	5.3 ± 0.03

Table II. Average of the shearing rate absolute value $\langle|\omega_{E\times B}|\rangle_{r,t}$ for $R_0/L_{T_0} = 6.9$.

ν_0^*	0	0.09	0.18	0.3	0.45
$\langle|\omega_{E\times B}|\rangle_{r,t}[10^{-2}c_s/a]$	10.2 ± 1.3	8.4 ± 0.4	9.5 ± 1.4	9.4 ± 0.5	9.5 ± 0.09

Figure 11 shows the profiles of the absolute $\vec{E}\times\vec{B}$ shearing rate values $|\omega_{E\times B}|(r)$, averaged over a time window of $200[a/c_s]$ in the quasi-stationary state of the turbulent simulation, for different collisionalities and for the temperature gradient $R_0/L_{T_0} = 5.3$. Figure 12 is similar to Figure 11 but considers the higher temperature gradient $R_0/L_{T_0} = 6.9$. In the Dimits shift region, i.e. at $R_0/L_{T_0} = 5.3$, the radially averaged shearing rates $\langle|\omega_{E\times B}|\rangle_r$ are close to the linear growth rate of the most unstable mode $\gamma_{max} \simeq 0.058[c_s/a]$. Furthermore, as mentioned above, the radially averaged shearing rate $\langle|\omega_{E\times B}|\rangle_r$ is only slightly affected by collisions. This is remarkable, given that the radial shearing rate profile $|\omega_{E\times B}|(r)$ is significantly modified when going from zero to finite collisionality. Note however the almost identical shape of $|\omega_{E\times B}|(r)$ for the two considered finite collisionalities $\nu_0^* = 0.09$ and $\nu_0^* = 0.18$. Above the Dimits shift region, i.e. at $R_0/L_{T_0} = 6.9$, $\gamma_{max} \simeq 0.156[c_s/a]$ is much larger than the collisionless shearing rate ($\langle|\omega_{E\times B}|\rangle_r \simeq 0.105[c_s/a]$), allowing the turbulence to survive and drive some anomalous transport. As for $R_0/L_{T_0} = 5.3$, the collisional zonal flows appear to be only slightly damped in the case $R_0/L_{T_0} = 6.9$. The shape of the profile $|\omega_{E\times B}|(r)$ is however affected by collisions and, unlike in the Dimits shift region, different collisionalities ($\nu_0^* = 0.09$ and $\nu_0^* = 0.18$) give different profiles $|\omega_{E\times B}|(r)$ for $R_0/L_{T_0} = 6.9$.

Note that ion-ion collisions generate neoclassical background flows through the neoclassical equilibrium electric field. For the collisionalities considered in this paper, the turbulence-driven flows are dominant compared to the neoclassical background flows, as shown in Figures 11 and 12. At very large collisionality, one may expect that the neoclassical shearing rate would become dominant, and thus that the turbulent transport would be reduced due to collisions. However, such a high collisionality range would be very far from the usual low collisionality of fusion-relevant tokamak plasmas that studying the system at even larger collision frequencies than those considered in this paper would not be of much interest.

The scan of considered temperature gradients is then extended at fixed collisionality, in order to sketch the dependence of the collisional heat diffusivity on the ion temperature gradient. Similarly to studies already done for the CYCLONE parameters in the frame of

collisionless simulations [25], Figure 13 shows how the ion temperature gradient affects the ion heat diffusivity for ITG turbulence at mid-radius $r/a = 0.5$, for the chosen collisionality $\nu^* = 0.09 = 2\nu^*_{\text{phys}}$. The blue plain line in Figure 13 is the fit to collisionless simulation results given in Ref. [25]. While the Dimits shift softening is again clearly illustrated by the difference between neoclassical diffusivity and total collisional diffusivity in the collisionless Dimits shift region ($4.5 \leqslant R_0/L_{T_0} < 6$), the collisional increase of the transport level is also emphasized in the region above the non-linear stability threshold ($R_0/L_{T_0} \geqslant 6$). Considering the same finite collisionality, Figure 14 shows respectively $\langle|\omega_{E\times B}|\rangle_{r,t}$ and γ_{max} for different values of the temperature gradient R_0/L_{T_0}. The end of the Dimits shift region, at approximately $R_0/L_{T_0} \simeq 6$, is characterized by a maximum growth rate γ_{max} becoming much larger than the averaged zonal flow level $\langle|\omega_{E\times B}|\rangle_{r,t}$. While the ITG γ_{max} increases linearly with the ion temperature gradient, the shearing rate level shows some saturation beyond the Dimits shift region due to a tertiary instability mechanism.

B. Mechanisms of the Dimits shift softening

In [12], the zonal flow damping by collisions is identified as the cause for a non vanishing collisional turbulent transport for $R_0/L_{T_0} = 5.3$, although the temperature gradient is in the Dimits shift region. A locally bursting behaviour of the zonal flow amplitude and related turbulent transport is presented. The bursting behaviour consists in periodic zonal flows damping by collisions, which in turn leads to an increase of the turbulence level and of the related turbulence transport. The increase of turbulence produces an increase of zonal flow level, until the next collisional damping. This general result is confirmed by simulations performed with the collisional version of ORB5 based on the parameters defined in Sec. II F for a narrow gradient profile, i.e. with $\Delta_{\mathcal{A}} = 0.15a$. Figure 15 shows the time evolution of the radial shearing rate profile $\omega_{E\times B}(r)$ for $\nu^*_0 = 0.3$, considering a narrow gradient profile with $R_0/L_{T_0} = 5.3$. Note that the observation of a clear bursting behaviour in ORB5 requires narrow gradients as those considered in this section. Bursting was much less obvious for the wider gradient simulation cases discussed in Sec. V A. As expected, transport is totally absent in a collisionless case, as shown in Figure 16 for $\nu^* = 0$, since the temperature gradient $R_0/L_{T_0} = 5.3$ is in the Dimits shift region, where the collisionless zonal flows are strong enough to quench the turbulence. Considering again $R_0/L_{T_0} = 5.3$ and two different

collisionalities $\nu^* \simeq 0.18$ and $\nu^* \simeq 0.3$ at the radial position $r/a = 0.45$, Figures 17 and 18 show the time evolution of the turbulent ion energy flux Q_{turb}, normalized with respect to its corresponding neoclassical value Q_{neo}, as well as the time evolution of the $\vec{E} \times \vec{B}$ shearing rate $\omega_{E\times B}$, normalized with respect to the growth rate of the most unstable mode $\gamma_{\max}$ in the linear phase of the simulation. A non-vanishing turbulent transport is established through collisions. The above mentioned bursting behaviour appears clearly in Figures 17 and 18: at an intermittance rate which is proportional to the collision frequency, the $\vec{E} \times \vec{B}$ shearing rate is damped, which in turn leads to an increase of the turbulent ion energy flux. The observation of a non-vanishing turbulent transport implies that the Dimits shift region of ion temperature gradients is softened by collisions. As already mentioned, the observed bursting behaviour is not easily identified if the gradient profiles are larger, as for instance in Sec. V A, maybe due to interaction of this bursting behaviour happening at different uncorrelated times at different radii, leading to a less coherent evolution of the system. The underlying mechanisms of turbulence-driven zonal flow damping are however probably the same, leading to an increase of the diffusivity with collisions for all gradient widths.

VI. RELEVANCE OF THE PITCH ANGLE SCATTERING APPROXIMATION

Some gyrokinetic codes [11] do not pay much attention to the collisions in the frame of turbulence studies and only consider pitch-angle operators. The linearized Landau operator implemented in ORB5 for self-collisions, described in detail in [10], accounts for pitch angle and energy diffusion, and thanks to its approximated background reaction term it ensures all the essential conservation and symmetry properties. It is thus clearly a more realistic operator in this respect than a mere pitch angle scattering operator (Lorentz approximation). A pitch angle scattering operator for electron-ion collisions, acting only through random kicks for markers in the pitch angle variable, is also implemented in ORB5 and described in full detail in [10]. Such an operator is clearly relevant for simulating the collisions of electrons on ions, due to the important mass ratio m_i/m_e between the two species. Such a mass ratio argument clearly does not apply for ion-ion collisions, which are thus very different from electron-ion collisions, and the use of a pitch angle scattering operator for ion-ion collisions may be questioned. Using a Lorentz operator in order to account for self-collisions is equivalent to considering a linearized Landau self-collision operator without the

background reaction term $C[\delta f_{LM}, f_{LM}]$ and without the energy diffusion term, such that the simplified self-collision operator reads (see Eq. (31) in Ref. [10]):

$$\hat{C}(\delta f_{LM}) = \frac{\nu_D(v)}{2}\hat{L}^2\delta f_{LM} = \frac{\nu_{ii}K(\mathsf{v})}{4\mathsf{v}^2}\hat{L}^2\delta f_{LM}, \tag{49}$$

where $\mathsf{v} = v/v_{th}$, $\hat{L}^2 = \partial/\partial\xi(1-\xi^2)\partial/\partial\xi$ is the Lorentz operator and

$$K(\mathsf{v}) = \left[(\mathsf{v}^2-1)\mathrm{erf}(\mathsf{v}/\sqrt{2}) + \sqrt{2/\pi}\ \mathsf{v}e^{-\mathsf{v}^2/2}\right]/\mathsf{v}^3 \tag{50}$$

is a Rosenbluth potential related function.

Considering the standard CYCLONE case with $R_0/L_{T_0} = 5.3$, a turbulent run started from a neoclassical equilibrium at high collisionality $\nu_0^* \simeq 0.71$ is first studied. As expected, the neoclassical equilibrium to which the system settles with the Lorentz operator (49) is different from the equilibrium with the full self-collision operator (1). The neoclassical kinetic energy flux predicted by the Lorentz operator is for instance larger than the neoclassical kinetic energy flux predicted by the Landau self-collision operator, as shown in Figure 19. Note that the neoclassical electric field is in some sense inconsistent in the case of the Lorentz operator, since the Lorentz operator does not conserve parallel momentum and thus leads to a neoclassical ion flux which is unphysical for self-collisions. The neoclassical electric field, settled for ensuring a vanishing ion flux in order to satisfy the quasi-neutrality equation with adiabatic electrons, is thus distorted by the unphysical particle flux of the Lorentz operator. However, the use of the Lorentz operator in the frame of turbulence studies seems to be roughly justified. Despite indeed evident neoclassical discrepancies, the time averaged turbulent kinetic energy flux at mid-radius $r/a = 0.5$ remains comparable between the operators, $\langle Q_{\text{turb, Lorentz}}\rangle_{\text{time}}/\langle Q_{\text{turb, self-coll}}\rangle_{\text{time}} = 1.14$. Considering the statistical uncertainty, this deviation is probably not significant. Figure 20 shows the evolution in time of the turbulent kinetic energy flux at mid-radius $r/a = 0.5$ for both operators.

In order to reduce the importance of the neoclassical transport compared to the turbulent transport, the gradient $R_0/L_{T_0} = 6.9$ is then chosen, along with a weaker collisionality $\nu_0^* = 0.14$. The simulation is carried out in this latter case without any neoclassical initialization phase. Figure 21 shows the evolution in time of the turbulent heat diffusivity $\chi_{turb} = Q_{turb}/n|\nabla T|$, averaged between $r/a = 0.4$ and $r/a = 0.6$, for both operators. The difference

is obviously small, at least in a time-averaged sense: $\langle \chi_{\text{turb, Lorentz}} \rangle_{\text{time}} / \langle \chi_{\text{turb, self-coll}} \rangle_{\text{time}} = 1.05$. The discrepancy is again probably not significant relatively to the statistical error.

VII. CONCLUSION

The issue of ion-ion collision effects on electrostatic ITG turbulent transport has been addressed through robust collision algorithms implemented in the global gyrokinetic code ORB5. Systematically starting turbulence simulations from a neoclassical equilibrium, which has not been done previously to our knowledge, a general increase in ion heat transport due to collisions has been observed in agreement with previous studies within the frame of the adiabatic electron model. The sources of the increased transport are neoclassical contributions and turbulent contributions via interactions between collisions and zonal flows, which have been emphasized and studied for different ion temperature gradients. The Dimits shift softening by collisions [12] has been characterized for the CYCLONE base case thanks to systematic scan over collisionality ν^* and ion temperature gradient R_0/L_{T_i}. The bursting behaviour of the collisional turbulent transport in the collisionless Dimits shift region has been discussed.

The tool for controlling the numerical noise in collisional turbulent simulations with ORB5, the coarse-graining procedure [9], [10], has been presented and its positive effects on the relevance of studies related to collisional turbulence have been pointed out.

Finally, for both neoclassical and turbulence simulations, the Lorentz approximation for self-collisions has been tested against the linearized Landau self-collision operator in ORB5, which accounts for energy diffusion and for local conservation of density, parallel momentum and kinetic energy. While a physically accurate self-collision operator is required in order to predict correctly the neoclassical transport, the Lorentz approximation captures essentially the features of the turbulent collisional transport in ITG regimes. However, the wrong predictions given by the Lorentz approximation for the neoclassical transport due to ion-ion collisions lead to a slight lack of accuracy in estimating the total transport.

Acknowledgements

Simulations were performed on the Monte Rosa CRAY XT-5 supercomputer of the Swiss

National Supercomputing Center, the HPC-FF cluster of the Jülich Forschungszentrum and the BlueGene/P supercomputer of the CADMOS project. This work was partly supported by the Swiss National Science Foundation. Two of the authors (T.V. & S.B.) would like to thank Per Helander and Clemente Angioni for useful discussions related to neoclassical transport and collision operators.

Appendix A: About the potential energy flux

The generic term *heat flux* is often used in order to qualify the quantity which is strictly the *kinetic energy flux*. Actually, the proper heat flux, as defined in Eq. (34), should also account for a potential energy flux [23] and a particle flux contribution. In the frame of simulations with adiabatic electrons, the total particle flux does vanish in order to ensure the ambipolarity condition, but the potential energy flux does not in collisional runs. In this paper one gives an estimate of the potential energy flux magnitude compared to the kinetic energy flux magnitude, the only term usually retained in the heat flux computation. ORB5 simulations show that the net potential energy flux is due mainly to the neoclassical Maxwellian contribution:

$$Q_{pot} \approx \left\langle \frac{1}{|\vec{\nabla}\Psi|} \int \mathrm{d}^3 v q \phi f_0 \left. \frac{\mathrm{d}\Psi}{\mathrm{d}t} \right|_0 \right\rangle_S . \tag{A1}$$

The potential energy flux (A1) is inward for the considered CYCLONE case, and has thus a balancing effect on the mainly outward kinetic energy flux. Considering a local Maxwellian background $f_0 = f_{LM}$, it is possible to show, by analytically expliciting the integral on the RHS of Eq. (A1), that the potential energy flux arises from the poloidal variation of the electrostatic potential:

$$Q_{pot} \approx 2\pi n_0 T_0 \frac{F(\Psi)}{S(\Psi)} \int_0^{2\pi} \frac{1}{B^2} \frac{\partial \phi}{\partial \theta^*} \mathrm{d}\theta^*, \tag{A2}$$

where $S(\Psi)$ is the flux surface defined by:

$$S(\Psi) = 2\pi \int_0^{2\pi} J_{\theta^* \Psi \varphi} |\vec{\nabla}\Psi| \mathrm{d}\theta^*. \tag{A3}$$

However, the magnitude of the total potential energy flux is small. For CYCLONE base case simulations with the temperature gradient $R_0/L_{T_0} = 6.9$, at $r/a = 0.5$ the scaling is found

empirically to be a quarter of the neoclassical kinetic energy flux, with opposite direction (pointing inwards):

$$\frac{Q_{pot}}{Q_{kin,neo}} \approx -\frac{1}{4}. \tag{A4}$$

[1] Z. Lin, T. S. Hahm, W. W. Lee, W. M. Tang, and R. B. White, Science **281** 1835 (1998).

[2] R. E. Waltz, R. L. Dewar, and X. Garbet, Phys. Plasmas **5**, 1784 (1998).

[3] P. H. Diamond, S.-I. Itoh, K. Itoh, and T. S. Hahm, Plasma Phys. Controlled Fusion **47**, R35 (2005).

[4] X. Garbet, Y. Idomura, L. Villard, and T. H. Watanabe, Nucl. Fusion **50**, 043002 (2010).

[5] F. L. Hinton and M. N. Rosenbluth, Plasma Phys. Controlled Fusion **41**, A653 (1999).

[6] S. Jolliet, A. Bottino, P. Angelino, R. Hatzky, T. M. Tran, B. F. McMillan, O. Sauter, K. Appert, Y. Idomura, and L. Villard, Comput. Phys. Commun. **177**, 409 (2007).

[7] B. F. McMillan, S. Jolliet, T. M. Tran, L. Villard, A. Bottino, and P. Angelino, Phys. Plasmas **15**, 052308 (2008).

[8] S. Brunner, E. Valeo, and J. A. Krommes, Phys. Plasmas **6**, 4504 (1999).

[9] Y. Chen and S. E. Parker, Phys. Plasmas **14**, 082301 (2007).

[10] T. Vernay, S. Brunner, L. Villard, B. F. McMillan, S. Jolliet, T. M. Tran, A. Bottino, and J. P. Graves, Phys Plasmas **17**, 122301 (2010).

[11] J. Candy, and R. E. Walz, Journal of Comp. Phys. **186**, 545 (2003).

[12] Z. Lin, T. S. Hahm, W. W. Lee, W. M. Tang, and P. H. Diamond, Phys. Rev. Lett. **83**, 3648 (1999).

[13] G. Dif-Pradalier, V. Grandgirard, Y. Sarazin, X. Garbet, and Ph. Ghendrih, Phys. Rev. Lett. **103**, 065002 (2009).

[14] R. E. Waltz, J. Candy, F. L. Hinton, C. Estrada-Mila, and J. E. Kinsey, Nucl. Fusion **45**, 741 (2005).

[15] P. Ricci, B. N. Rogers, and W. Dorland, Phys. Rev. Lett. **97**, 245001 (2006).

[16] D. R. Mikkelsen, W. Dorland, Phys. Rev. Lett. **101**, 135003 (2008).

[17] Z. Lin, W. M. Tang, and W. W. Lee, Phys. Plasmas **2**, 2975 (1995).

[18] T. S. Hahm, Phys. Fluids **31**, 2670 (1988).

[19] P. Angelino, A. Bottino, R. Hatzky, S. Jolliet, O. Sauter, T. M. Tran, and L. Villard, Phys. Plasmas **13**, 052304 (2006).

[20] S. J. Allfrey, R. Hatzky, Comp. Phys. Commun. **154**, 98 (2003).

[21] S. Satake, R. Kanno, and H. Sugama, Plasma Fusion Res. **3** (2008).

[22] B .F. McMillan, S. Jolliet, A. Bottino, P. Angelino, T. M. Tran, and L. Villard, Comp. Phys. Commun. **181**, 715 (2010).

[23] P. Helander, Plasma Phys. Controlled Fusion, **37**, 57 (1995).

[24] X. Lapillonne, S. Brunner, T. Dannert, S. Jolliet, A. Marinoni, L. Villard, T. Görler, F. Jenko, and F. Merz, Phys. Plasmas **16**, 032308 (2009).

[25] A. M. Dimits, G. Bateman, M. A. Beer, B. I. Cohen, W. Dorland, G. W. Hammett, C. Kim, J. E. Kinsey, M. Kotschenreuther, A. H. Kritz, L. L. Lao, J. Mandrekas, W. M. Nevins, S. E. Parker, A. J. Redd, D. E. Shumaker, R. Sydora, and J. Weiland, Phys. Plasmas **7**, 969 (2000).

[26] S. Jolliet, PhD thesis, Ecole Polytechnique Fédérale de Lausanne (2009).

[27] M. N. Rosenbluth and F. L. Hinton, Phys. Rev. Lett. **80**, 724 (1998).

[28] C. S. Chang and F. L. Hinton, Phys. Fluids **25**, 1493 (1982).

[29] L. Villard, A. Bottino, O. Sauter, and J. Vaclavik, Phys. Plasmas **9**, 2684 (2002).

[30] B. N. Rogers, W. Dorland, and M. Kotschenreuter, Phys. Rev. Lett. **85**, 5336 (2000).

- Fig. 1: Field-aligned binning in configuration space represented respectively in the (θ^*, φ) plane, the (θ^*, z) plane and the (θ^*, s) plane.

- Fig. 2: (Color online) Evolution in time of the energy $E^{(n)}$ of two toroidal Fourier modes ($n = 10$ and $n = 44$), for different coarse-graining parameters, in the linear phase and the early non-linear phase of the simulation. An appropriate choice for the coarse-graining binning parameters allows to preserve the linear growth rate of the modes, while too large bins lead to an important non-physical energy dissipation.

- Fig. 3: Time evolution of the signal-to-noise ratio considering the coarse-graining procedure switched off (plain lines) and on (dash-dotted lines) respectively, both for 90×10^6 (grey lines) and 180×10^6 (black lines) markers. The coarse-graining method is crucial in order to carry out simulations above the SNR threshold of relevance (~ 10).

- Fig. 4: (Color online) Rosenbluth-Hinton test where no gradients are considered: time evolution of the radial electric field E_r at mid-radius for both collisionless and collisional simulations. The collisionless residual depends on the initial amplitude of the perturbation $\delta f / f_{LM}$, while the collisional residual does always vanish. Time is normalized by the GAM frequency ω_g.

- Fig. 5: (Color online) Rosenbluth-Hinton test where the CYCLONE case gradients ($R_0/L_{n_0} = 2.2$, $R_0/L_{T_0} = 6.9$) are considered: time evolution of the radial electric field E_r at mid-radius for both collisionless and collisional simulations. The collisionless residual depends on the initial amplitude of the perturbation $\delta f / f_{LM}$, while the collisional residual converges towards the neoclassical equilibrium value, regardless of the initial perturbation. Time is normalized by the GAM frequency ω_g.

- Fig. 6: (Color online) Time evolution of the neoclassical (red dashed line) and turbulent (blue plain line) contributions to the kinetic energy flux Q_{kin} at mid-radius, in the neoclassical phase and the turbulent phase of the simulation respectively, for $\nu_0^* = 0.18$. Once a neoclassical equilibrium is established, turbulence is switched on and turbulent transport becomes dominant compared to neoclassical transport, for CYCLONE case gradients ($R_0/L_{n_0} = 2.2$, $R_0/L_{T_0} = 6.9$). The neoclassical flux is perturbed by turbulence but remains constant in a time-averaged sense.

- Fig 7: (Color online) Heat diffusivity χ_H at mid-radius versus the collisionality parameter ν^*, for both temperature gradients $R_0/L_{T_0} = 5.3$ (blue crosses) and $R_0/L_{T_0} = 6.9$ (black squares). The contribution of the neoclassical diffusivity (red circles) to the total diffusivity is important for the weaker gradient $R_0/L_{T_0} = 5.3$, while it becomes marginal for the larger gradient $R_0/L_{T_0} = 6.9$. The total diffusivity, increasing with collisions, is in general larger than the mere neoclassical diffusivity added to the collisionless turbulent diffusivity.

- Fig. 8: (Color online) Heat diffusivity profile $\chi_H(r)$ in the quasi-stationary state of the simulation, for a collisionality $\nu_0^* = 0.45$ and both temperature gradients $R_0/L_{T_0} = 5.3$ and $R_0/L_{T_0} = 6.9$. For the weaker gradient $R_0/L_{T_0} = 5.3$, the turbulent contribution profile (blue crosses) is similar to the neoclassical contribution profile (red plain line), while the turbulent contribution profile in the case of the larger gradient $R_0/L_{T_0} = 6.9$ (black squares) is clearly dominant, even for a collisionality ten times larger than the physical one $\nu^*_{0,\mathrm{phys}} \simeq 0.045$. The neoclassical contribution is successfully benchmarked against the Chang-Hinton predictions (green dashed line).

- Fig. 9: (Color online) Time evolution of the $\omega_{E\times B}$ shearing rate profile, considering a collisionality $\nu_0^* = 0.18$ and a temperature gradient $R_0/L_{T_0} = 5.3$. The temperature and density gradients are non-zero from $r/a = 0.2$ to $r/a = 0.8$ (wide-shaped profiles, $\Delta_{\mathcal{A}} = 0.3$). The limited turbulence drive leads to a quiescent evolution of the zonal flows.

- Fig. 10: (Color online) Time evolution of the $\omega_{E\times B}$ shearing rate profile, considering a collisionality $\nu_0^* = 0.18$ and a temperature gradient $R_0/L_{T_0} = 6.9$. The temperature and density gradients are non-zero from $r/a = 0.2$ to $r/a = 0.8$ (wide-shaped profiles, $\Delta_{\mathcal{A}} = 0.3$). The strong turbulence drive leads to zonal flow variations on short time scales in the quasi-stationary state of the simulation.

- Fig. 11: (Color online) Profiles of the $\vec{E} \times \vec{B}$ shearing rate absolute value $|\omega_{E\times B}|(r)$ for different collisionalities and a temperature gradient $R_0/L_{T_0} = 5.3$, the neoclassical contributions being emphasized. The averaged shearing rate level is of the order of the growth rate of the most unstable mode γ_{max} (grey dashed line). The zonal flow damping by collisions is possibly balanced by an additional turbulence drive. For the

considered collisionalities, the turbulence-driven zonal flows are dominant compared to the neoclassical flows.

- Fig. 12: (Color online) Profiles of the $\vec{E} \times \vec{B}$ shearing rate absolute value $|\omega_{E\times B}|(r)$ for different collisionalities and a temperature gradient $R_0/L_{T_0} = 6.9$, the neoclassical contributions being emphasized. The averaged shearing rate level is much smaller than the growth rate of the most unstable mode γ_{max} (grey dashed line). The collisional zonal flows appear to be slightly damped, but nevertheless driven to a non-vanishing value, possibly by an additional turbulence drive. For the considered collisionalities, the turbulence-driven zonal flows are dominant compared to the neoclassical flows.

- Fig. 13: (Color online) Heat diffusivity χ_H at mid-radius versus the temperature gradient R_0/L_{T_0}. The blue plain line is the collisionless prediction resulting from an empirical fit on gyrokinetic simulation results. For $\nu_0^* = 0.09$, the red dashed line shows the neoclassical diffusivity level and the green diamonds represent the total diffusivity for different temperature gradients. Collisions clearly increase the heat diffusivity and soften the so-called Dimits shift region.

- Fig. 14: (Color online) Maximum linear growth rate γ_{max} (black crosses) and averaged shearing rate $\langle|\omega_{E\times B}|\rangle_{r,t}$ (red squares) for different temperature gradients R_0/L_{T_0} and for the finite collisionality $\nu_0^* = 0.09$. Beyond the Dimits shift region, $\gamma_{max} > \langle|\omega_{E\times B}|\rangle_{r,t}$. The saturation of the shearing rate level is due to a tertiary instability mechanism.

- Fig. 15: (Color online) Time evolution of the $\omega_{E\times B}$ shearing rate profile, considering a collisionality $\nu_0^* = 0.3$ and a temperature gradient $R_0/L_{T_0} = 5.3$. The temperature and density gradients are non-zero from $r/a = 0.35$ to $r/a = 0.65$ (narrow-shaped profiles, $\Delta_{\mathcal{A}} = 0.15$). The bursting evolution of the zonal flows is visible.

- Fig. 16: For a collisionless simulation and a narrow temperature gradient with $R_0/L_{T_0} = 5.3$, time evolution of both the heat diffusivity χ_H (black plain line) and the $\vec{E} \times \vec{B}$ shearing rate $\omega_{E\times B}$ (grey dash-dotted line) at mid-radius. $\omega_{E\times B}$ reaches a quasi-stationary value comparable to the linear growth rate of the most unstable mode γ_{max} (grey dashed line), quenching totally the turbulence and leading to a vanishing heat transport.

- Fig. 17: For $\nu_0^* = 0.18$ and a narrow temperature gradient with $R_0/L_{T_0} = 5.3$, time evolution of both the kinetic energy flux generated by turbulence $Q_{\rm turb}$ (black plain line) and the $\vec{E} \times \vec{B}$ shearing rate $\omega_{E\times B}$ (grey dash-dotted line) at $r/a = 0.45$. The periodic damping of the zonal flows by collisions leads in turn to periodic bursts in the heat transport, at a rate proportional to the collision frequency.

- Fig. 18: Same representation as in Fig. 17 for $\nu_0^* = 0.3$, leading to the same conclusions. The periodicity of the observed bursting behaviour is again related to the collision frequency.

- Fig. 19: For $\nu_0^* \simeq 0.71$ and $R_0/L_{T_0} = 5.3$, neoclassical kinetic energy flux profile due to ion-ion collisions $Q_{\rm neo}(s)$ predicted by both the Lorentz operator (grey dashed line) and the Landau self-collision operator (black plain line). The Lorentz approximation is not accurate enough in order to describe correctly the neoclassical transport due to self-collisions.

- Fig. 20: For $\nu_0^* \simeq 0.71$ and $R_0/L_{T_0} = 5.3$, time evolution of the turbulent kinetic energy flux $Q_{\rm turb}$ at mid-radius predicted by both the Lorentz operator (grey dashed line) and the Landau self-collision operator (black plain line). Despite visible discrepancies, the level of turbulent transport is approximately described by the Lorentz operator in a time-averaged sense.

- Fig. 21: For $\nu_0^* \simeq 0.14$ and $R_0/L_{T_0} = 6.9$, time evolution of the turbulent heat diffusivity $\chi_{\rm turb}$ averaged between $r/a = 0.4$ and $r/a = 0.6$, predicted by both the Lorentz operator (grey dashed line) and the Landau self-collision operator (black plain line). The turbulent transport level in a time-averaged sense is accurately described by the Lorentz operator.

Fig. 1

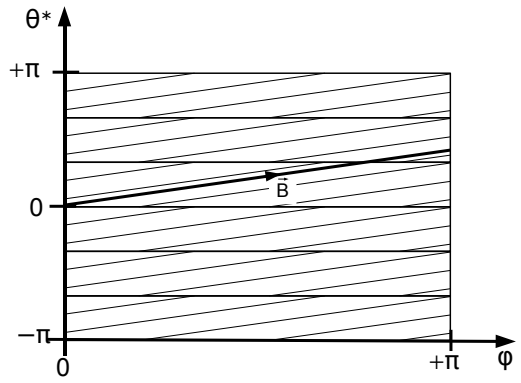

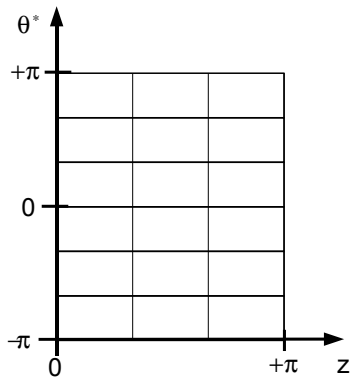

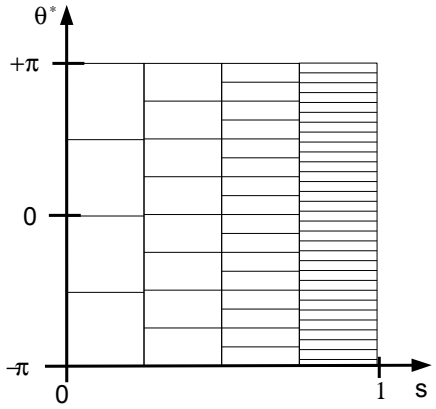

Fig. 2

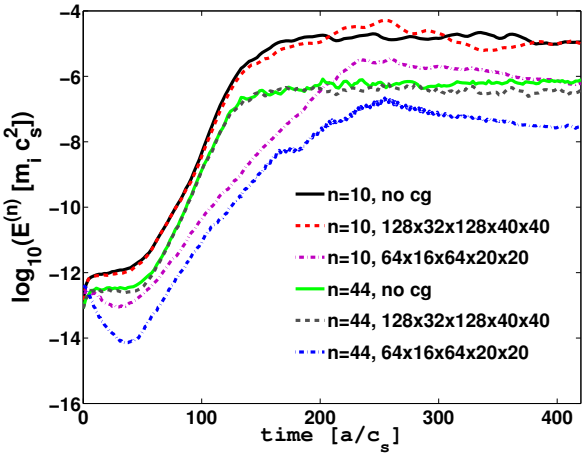
log10(E(n) [mi cs2])
time [a/cs]
n=10, no cg
n=10, 128x32x128x40x40
n=10, 64x16x64x20x20
n=44, no cg
n=44, 128x32x128x40x40
n=44, 64x16x64x20x20
−4
−6
−8
−10
−12
−14
−16
0
100
200
300
400

Fig. 3

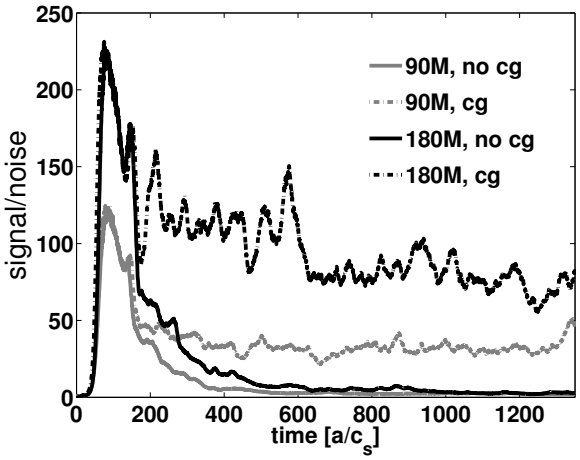
250
200
150
100
50
0
signal/noise
0
200
400
600
800
1000
1200
time [a/c_s]
90M, no cg
90M, cg
180M, no cg
180M, cg

Fig. 4

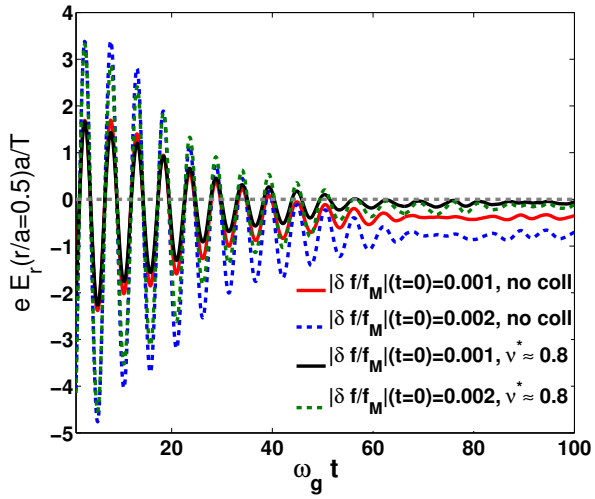
e E_r(r/a=0.5)a/T
ω_g t
|δ f/f_M|(t=0)=0.001, no coll
|δ f/f_M|(t=0)=0.002, no coll
|δ f/f_M|(t=0)=0.001, ν* ≈ 0.8
|δ f/f_M|(t=0)=0.002, ν* ≈ 0.8

Fig. 5

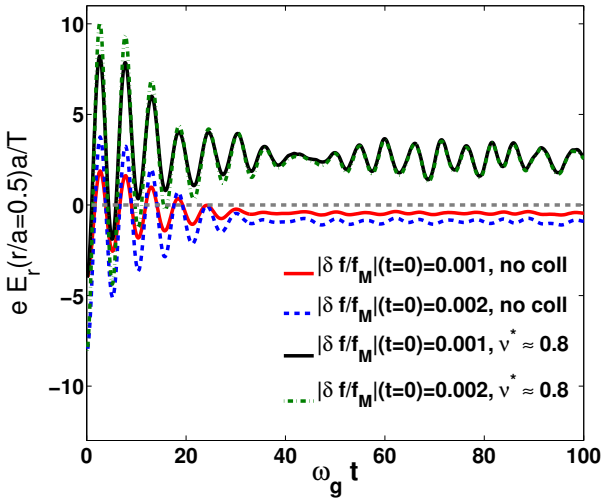
10
5
0
−5
−10
0
20
40
60
80
100
ω_g t
e E_r(r/a=0.5)a/T
|δ f/f_M|(t=0)=0.001, no coll
|δ f/f_M|(t=0)=0.002, no coll
|δ f/f_M|(t=0)=0.001, ν* ≈ 0.8
|δ f/f_M|(t=0)=0.002, ν* ≈ 0.8

Fig. 6

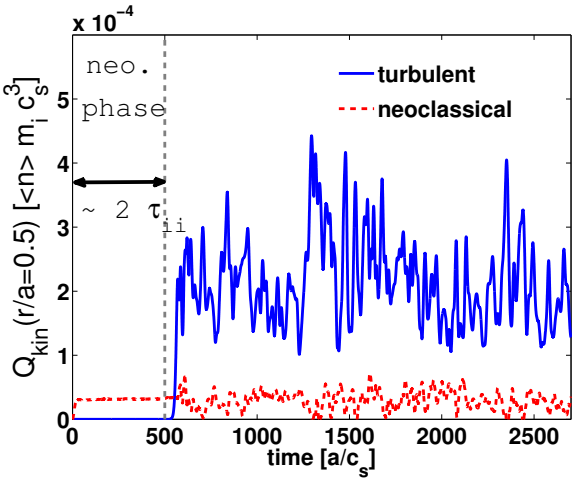
x 10^-4
neo.
phase
~ 2 τii
turbulent
neoclassical
Qkin(r/a=0.5) [<n> mi cs^3]
time [a/cs]
0
1
2
3
4
5
0
500
1000
1500
2000
2500

Fig. 7

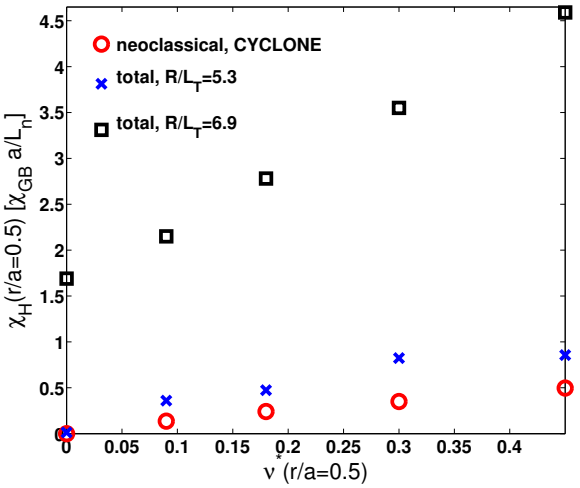
neoclassical, CYCLONE
total, R/L_T=5.3
total, R/L_T=6.9
χ_H(r/a=0.5) [χ_GB a/L_n]
ν (r/a=0.5)
0
0.5
1
1.5
2
2.5
3
3.5
4
4.5
0.05
0.1
0.15
0.2
0.25
0.3
0.35
0.4

Fig. 8

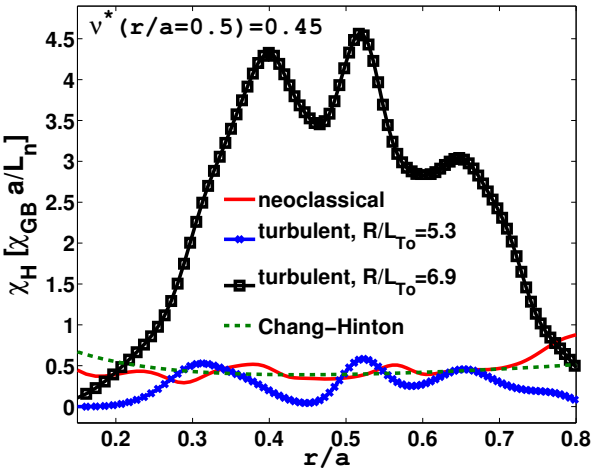
ν*(r/a=0.5)=0.45
neoclassical
turbulent, R/L_To=5.3
turbulent, R/L_To=6.9
Chang–Hinton
χ_H [χ_GB a/L_n]
r/a
0
0.5
1
1.5
2
2.5
3
3.5
4
4.5
0.2
0.3
0.4
0.5
0.6
0.7
0.8

Fig. 9

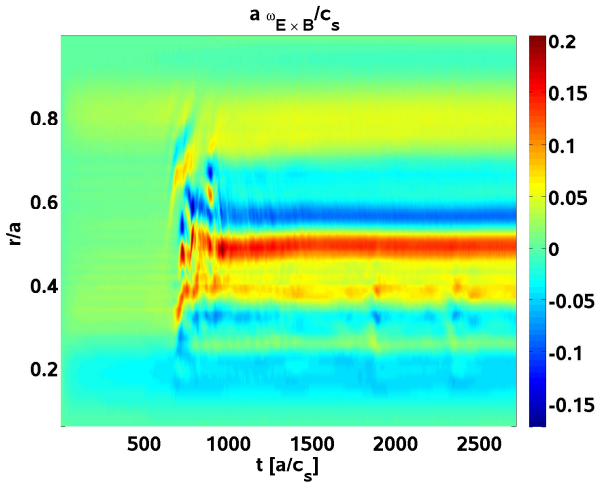
a ω_E×B/c_s
0.8
0.6
0.4
0.2
r/a
500
1000
1500
2000
2500
t [a/c_s]
0.2
0.15
0.1
0.05
0
-0.05
-0.1
-0.15

Fig. 10

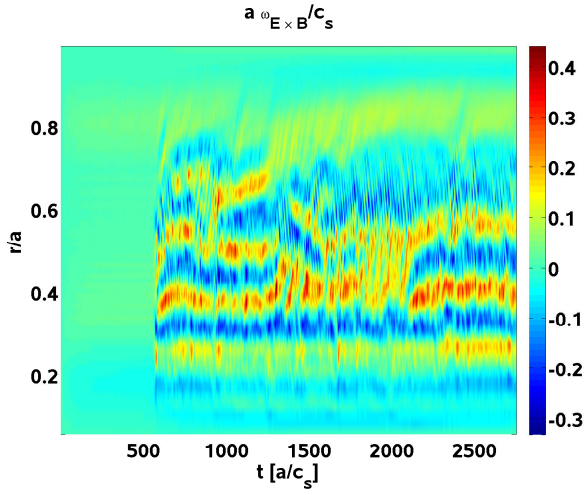
a ω_E×B/c_s
0.8
0.6
0.4
0.2
r/a
500
1000
1500
2000
2500
t [a/c_s]
0.4
0.3
0.2
0.1
0
-0.1
-0.2
-0.3

Fig. 11

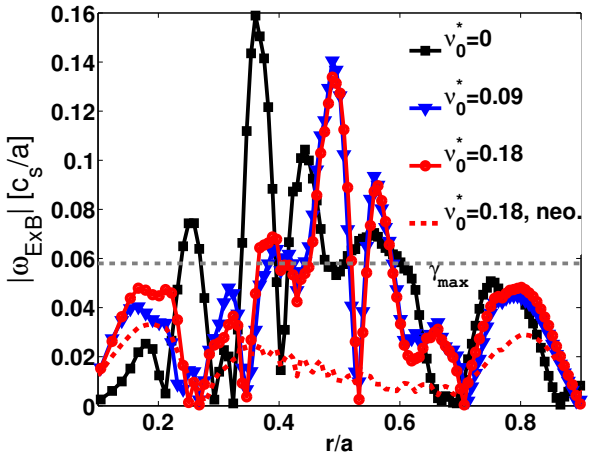
0.16
0.14
0.12
0.1
0.08
0.06
0.04
0.02
0
0.2
0.4
0.6
0.8
r/a
$|\omega_{ExB}|$ [c_s/a]
ν_0^*=0
ν_0^*=0.09
ν_0^*=0.18
ν_0^*=0.18, neo.
γ_{max}

Fig. 12

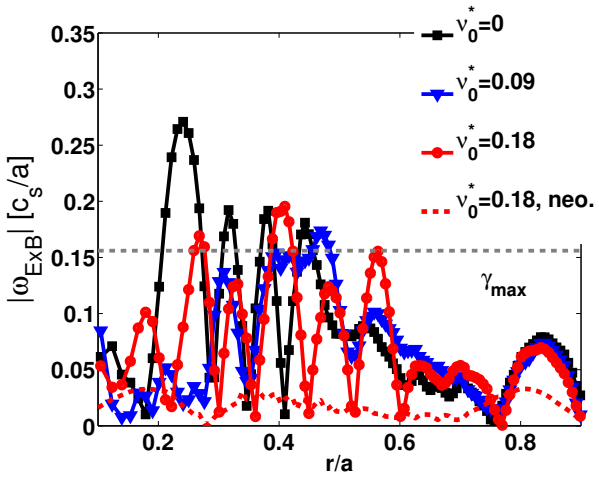
0.35
0.3
0.25
0.2
0.15
0.1
0.05
0
0.2
0.4
0.6
0.8
r/a
|ω_ExB| [c_s/a]
ν*_0=0
ν*_0=0.09
ν*_0=0.18
ν*_0=0.18, neo.
γ_max

Fig. 13

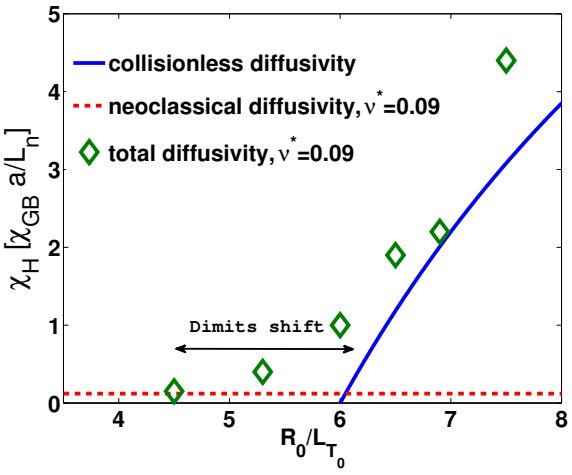
collisionless diffusivity
neoclassical diffusivity, ν*=0.09
total diffusivity, ν*=0.09
Dimits shift
χH [χGB a/Ln]
R0/LT0
0
1
2
3
4
5
4
5
6
7
8

Fig. 14

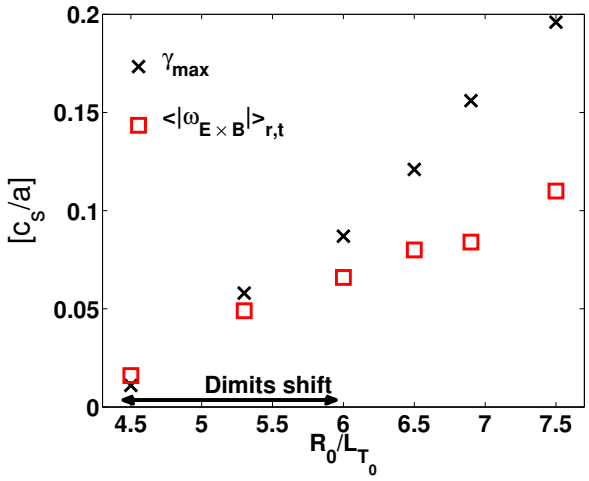
0.2
0.15
0.1
0.05
0
[c_s/a]
γ_max
<|ω_E×B|>_r,t
Dimits shift
4.5
5
5.5
6
6.5
7
7.5
R_0/L_T_0

Fig. 15

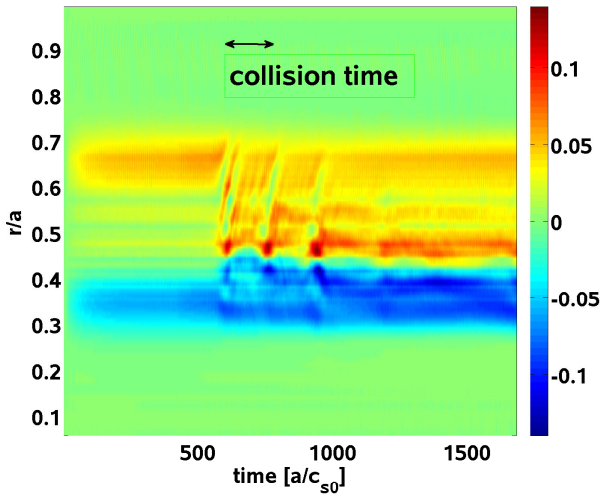
collision time
r/a
0.9
0.8
0.7
0.6
0.5
0.4
0.3
0.2
0.1
500
1000
1500
time [a/c_s0]
0.1
0.05
0
-0.05
-0.1

Fig. 16

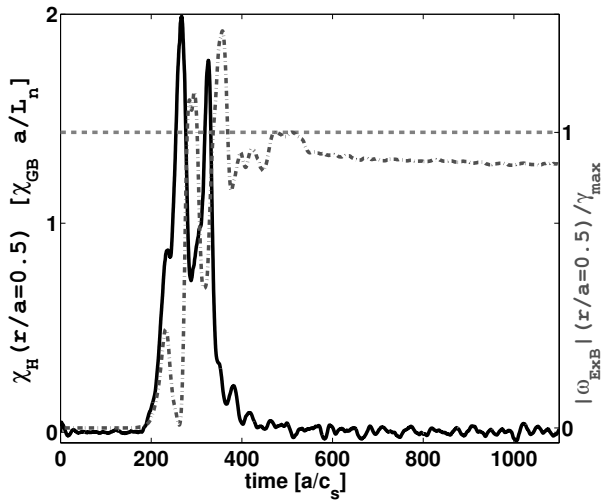
2
1
0
0
200
400
600
800
1000
time [a/c_s]
χ_H (r/a=0.5) [χ_GB a/L_n]
|ω_ExB| (r/a=0.5)/γ_max
1
0

Fig. 17

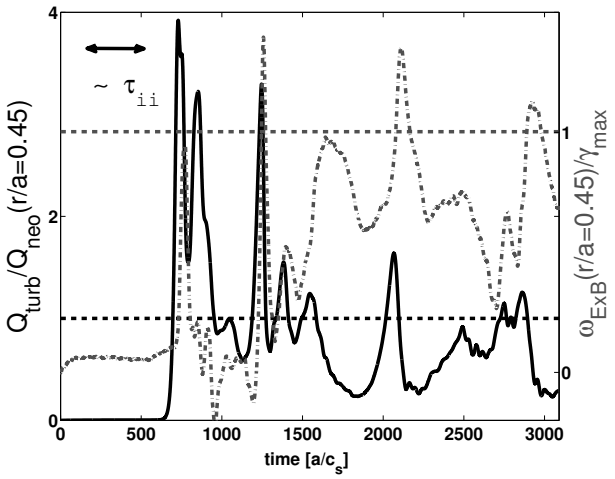
~ τii
Qturb/Qneo(r/a=0.45)
ωExB(r/a=0.45)/γmax
time [a/cs]
0
500
1000
1500
2000
2500
3000
0
2
4
1
0

Fig. 18

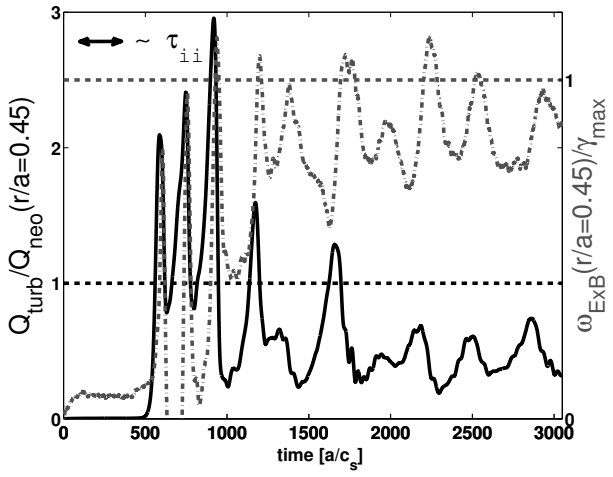
~ τii
Qturb/Qneo(r/a=0.45)
ωExB(r/a=0.45)/γmax
time [a/cs]
0
500
1000
1500
2000
2500
3000
1
2
3

Fig. 19

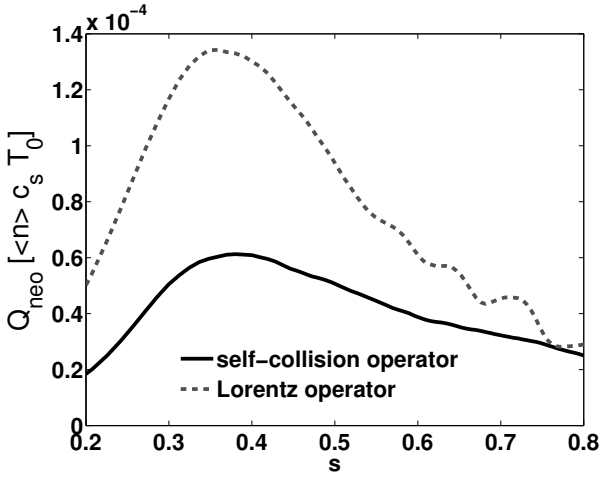
x 10^-4
1.4
1.2
1
0.8
0.6
0.4
0.2
0
Q_neo [<n> c_s T_0]
0.2
0.3
0.4
0.5
0.6
0.7
0.8
s
self−collision operator
Lorentz operator

Fig. 20

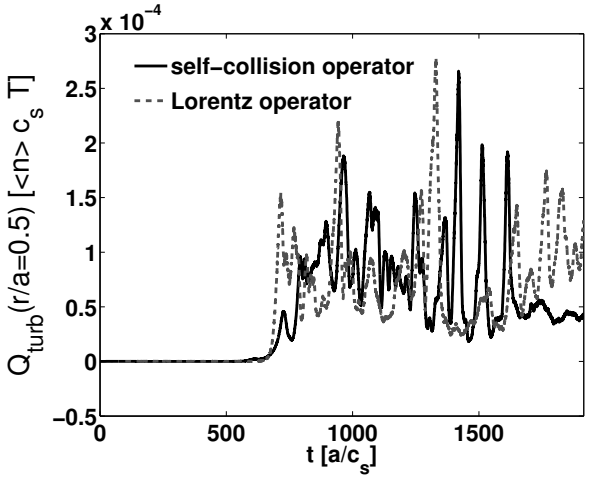
x 10^−4
3
2.5
2
1.5
1
0.5
0
−0.5
0
500
1000
1500
t [a/c_s]
Q_turb(r/a=0.5) [<n> c_s T]
self−collision operator
Lorentz operator

Fig. 21

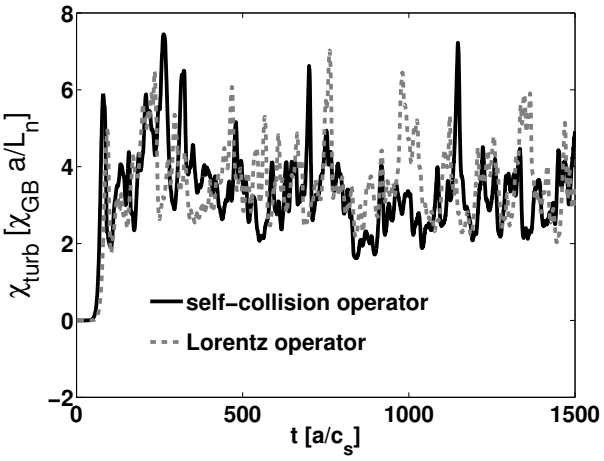
8
6
4
2
0
−2
0
500
1000
1500
χ_{turb} [χ_{GB} a/L_n]
t [a/c_s]
self−collision operator
Lorentz operator